Open access • Posted Content • DOI:10.1101/2021.05.26.445856

Structural mechanisms for gating and ion selectivity of the human polyamine transporter ATP13A2 — Source link

Jordan Tillinghast, Darren Bowser, Kenneth Pak Kin Lee

Institutions: Pennsylvania State University

Published on: 27 May 2021 - bioRxiv (Cold Spring Harbor Laboratory)

Topics: Polyamine transport, Polyamine binding, Spermine and Polyamine

Structural mechanisms for gating and ion selectivity of the human polyamine transporter ATP13A2

Jordan Tillinghast[1], Darren Bowser[1] & Kenneth Pak Kin Lee[1]*

Affiliations:

[1]Department of Cellular and Molecular Physiology, Pennsylvania State University College of Medicine, The Pennsylvania State University; Hershey, Pennsylvania, 17033, USA.

*Corresponding author. Email: kennethlee@psu.edu

Summary: Mutations in *ATP13A2*, also known as *PARK9*, cause a rare monogenic form of juvenile onset Parkinson's disease named Kufor-Rakeb syndrome and other neurodegenerative diseases. *ATP13A2* encodes a neuroprotective P5B P-type ATPase highly enriched in the brain that mediates selective import of spermine ions from lysosomes into the cytosol via an unknown mechanism. Here we present three structures of human ATP13A2 bound to an ATP analogue or to spermine in the presence of phosphomimetics determined by electron cryo-microscopy. ATP13A2 autophosphorylation opens a lysosome luminal gate to reveal a narrow lumen access channel that holds a spermine ion in its entrance. ATP13A2's architecture establishes physical principles underlying selective polyamine transport and anticipates a "pump-channel" intermediate that could function as a counter-cation conduit to facilitate lysosome acidification. Our findings establish a firm foundation to understand ATP13A2 mutations associated with disease and bring us closer to realizing ATP13A2's potential in neuroprotective therapy.

Keywords: ATP13A2, PARK9, P-type ATPase, cryo-EM, polyamine, ion transport, ion channel, ion selectivity, gating mechanism, Parkinson's disease

Highlights:

1. Structures of the Parkinson's disease-associated polyamine transporter ATP13A2
2. Structures of three transport cycle intermediates reveal the gating mechanism
3. Architecture of the polyamine binding site reveals mechanisms for ion selectivity
4. The polyamine binding site's location anticipates an ion channel-like mechanism

Introduction:

Polyamines are ubiquitous in biology (Michael, 2016). Regulation of cell proliferation, modulation of ion channel behavior and neuroprotection are among the numerous pleiotropic functions of polyamines (Clarkson et al., 2004; Pegg, 2016; Yang et al., 2017). In humans, disruptions in polyamine metabolism and transport have been associated with cancer, aging and neurodegenerative diseases (Madeo et al., 2018). Polyamine uptake in a mammalian system was first shown by Dykstra and Herbst in 1965 (Dykstra and Herbst, 1965). More than half a century later, ATP13A2 was compellingly demonstrated to be a human polyamine uptake transporter (van Veen et al., 2020). ATP13A2 is a member of the P5B family of P-type adenosine triphosphatases (P5B-ATPases) highly expressed in the brain (Palmgren and Nissen, 2011; Schultheis et al., 2004; Sorensen et al., 2018). Polyamine export from lysosomes mediated by ATP13A2 sets the resting cellular polyamine content and protects against mitochondrial oxidative stress (van Veen et al., 2020; Vrijsen et al., 2020); its deficit impairs lysosome function and promotes neuronal cell death (van Veen et al., 2020). Many loss-of-function mutations in the *ATP13A2* gene (also known as *PARK9*) have been causally linked to a large spectrum of neurodegenerative diseases including Kufor-Rakeb syndrome and early-onset Parkinson's disease (Bras et al., 2012; Di Fonzo et al., 2007; Estrada-Cuzcano et al., 2017; Klein and Westenberger, 2012; Lin et al., 2008; Ramirez et al., 2006; Spataro et al., 2019). Enhancement of ATP13A2 function has been proposed as a neuroprotective therapeutic strategy in Parkinson's disease (Dehay et al., 2012a; Dehay et al., 2012b; Park et al., 2015).

Under physiological conditions the natural polyamines: spermine (SPM), spermidine (SPD) and putrescine (PUT) exist as tetravalent, trivalent and divalent cations, respectively (Bergeron et al., 1995). ATP13A2 prefers spermine over spermidine though both are efficiently transported; it shows little activity toward putrescine and metal ions (van Veen et al., 2020). The observation that ATP13A2 is able to transport ions with variable charge and size is surprising since canonical metal ion P-type ATPases including sarcoendoplasmic reticulum Ca^{2+}-ATPase (SERCA) and Na^{+}/K^{+}-ATPase are highly selective ion pumps (Dyla et al., 2020; Morth et al., 2011). Given that acidic residues coordinating metal ions in SERCA and Na^{+}/K^{+}-ATPase are not conserved in ATP13A2 (Figure S1), we should expect to discover that ATP13A2 has evolved to handle polyamine ions using an alternate ion selection apparatus.

In addition to the question of ion selectivity, many fundamental aspects of polyamine transport by ATP13A2 remain to be characterized. What is the ion permeation pathway? What are the gating structures and how do they open and close? In the present study we address these questions by determining structures of human ATP13A2 representing three intermediates in its transport cycle using single-particle electron cryo-microscopy (cryo-EM). A biochemical analysis of structure-activity relationships among ATP13A2's polyamine substrates is also presented.

Results:

Biochemical characterization

We expressed full-length human ATP13A2 (hATP13A2) in a human embryonic kidney cell line and purified the recombinant ion pump in a detergent system containing dodecylmaltoside (DDM) and cholesteryl hemisuccinate (CHS) (Figures S2A and S2B). Purified hATP13A2 exhibited polyamine-dependent ATPase activity, in qualitative agreement with previous observations (Figures 1A and S2C) (van Veen et al., 2020). hATP13A2 is selective toward linear polyamines as the cyclic polyamine 1,4,8,11-tetraazacyclotetradecane (cyclam) did not stimulate hATP13A2 ATPase activity (Figures 1A and S2E).

Spermine-dependent ATPase activity of ATP13A2 is thought to be up-regulated by phosphatidic acid (PA) and phosphatidylinositol-(3,5)-bisphosphate ($PI(3,5)P_2$) (van Veen et al., 2020). We found that spermine robustly stimulated hATP13A2 ATPase activity without necessitating lipid supplementation (Figures 1A and S2C); $PI(3,5)P_2$ enhanced hATP13A2's catalytic output but PA did not (Figure 1B). We attribute the differential effects of PA between our study and that of van Veen et. al. to differences in protein source and purification methods (van Veen et al., 2020).

Structure determination and overall architecture

According to Post (Post et al., 1969) and Albers (Albers, 1967), ion transport by P-type ATPases can be understood as alternating cytosol-pump and extracellular milieu-pump ion exchange reactions mediated by four intermediates cycling in sequence: E1→E1P→E2P→E2 (Figure 1C). Intermediate states of hATP13A2 can be stabilized using the ATP analogue adenosine 5'-(β,γ-imido)-triphosphate (AMPPNP) and the phosphate analogues beryllium fluoride (BeF_3^-) and magnesium fluoride (MgF_4^{2-}). These inhibitors efficiently suppressed SPM-dependent hATP13A2

ATPase activity as expected (Figure S2D). We performed single-particle cryo-EM analysis of hATP13A2 complexed with: (i) AMPPNP (E1-AMPPNP); (ii) SPM plus BeF_3^- (SPM-E2-BeF_3^-) and (iii) SPM plus MgF_4^{2-} (SPM-E2-MgF_4^{2-}) (Figures 1C and S3A–S3F). The E1-AMPPNP structure represents ATP bound E1 (E1-ATP). The SPM-E2-BeF_3^- structure represents the substrate bound phosphoenzyme (SPM-E2P). The SPM-E2-MgF_4^{2-} structure represents the substrate bound dephosphorylated pump before PO_4^{3-} is ejected (SPM-E2-P_i). The three structures: E1-AMPPNP, SPM-E2-BeF_3^- and SPM-E2-MgF_4^{2-} were determined to resolutions of 2.9 Å, 2.7 Å and 3.0 Å, respectively (Figures S4E–S4G and Table S1).

A large transmembrane domain and a large multi-domain cytosolic headpiece comprise the hATP13A2 structures (Figures 1D, 1E, and S3D–S3F). The transmembrane regions of all three structures were similar in quality (Figures 1E, 3A, and S4H–S4J). The headpiece is most clearly resolved in the E1-AMPPNP structure, whose cryo-EM density was of excellent quality over most parts of the structure (Figures 1E and S4H). An atomic model of 1046 of 1180 residues in the hATP13A2 polypeptide sequence was built into the E1-AMPPNP cryo-EM map *de novo* (Figures 1E and 1F), which was then used as a template to build the SPM-E2-BeF_3^- and SPM-E2-MgF_4^{2-} structures.

A fold typical of P-type ATPases constitutes the core of hATP13A2 (Figure 1F). This core consists of ten transmembrane helices M1 through M10 and three cytosolic domains named: actuator (A), nucleotide binding (N) and phosphorylation (P) that make up the tripartite headpiece (Figures 1D–1F). The hATP13A2 core is flanked by two extensions: the N-terminal domain (NTD, aa. 1 to 186) embedded in the membrane inner leaflet (Figures 1D, S5A and S5B) and the C-terminal domain

(CTD, aa. 1151 to 1180) (Figures 1D and 1F). Strong conservation of sequence indicates that both the NTD and CTD are structural signatures throughout the P5B-ATPase family (Figure S1).

Functional implications of ATP13A2 extension domains

ATP13A2 is known to readily undergo autophosphorylation (Holemans et al., 2015; van Veen et al., 2020). This is not surprising since this step is expected to license ATP13A2 to sample "outward-open" conformations to access the lysosome lumen. How can the propensity of ATP13A2 to phosphorylate itself be explained from a physical perspective? In the autophosphorylated E2P state SERCA's A domain positions Glu183 in the conserved TGES loop near the phosphorylated Asp351 sidechain in the P domain to catalyze Asp351's dephosphorylation (Figure S1) (Olesen et al., 2007). The hATP13A2 E1-AMPPNP structure shows that the NTD anchors and pulls the A domain toward the inner leaflet of the lipid bilayer (Figure 2A). The resulting effect is the placement of the TGES loop in the hATP13A2 A domain ~200% closer to the phosphorylated aspartic acid residue in the P domain (Asp513) compared to the analogous distance in the SERCA E1-AMPPCP structure (Figure 2A). The predisposition of ATP13A2 to autophosphorylate under physiological ATP settings can thus be understood simply as a reflection of a forward bias imposed by the NTD to attain the E2P conformation.

To identify the location of the PA/PI(3,5)P_2 binding site we consider the surface electrostatics of hATP13A2, which shows an extensive positively charged pocket located at bilayer-water interface near the CTD (Figure 2B). Strong cryo-EM density resembling the headgroup and glycerol backbone of a bound phospholipid molecule is present in the cationic pocket (Figure 2B). The

exact identity of the occupant phospholipid remains to be determined and it likely corresponds to a co-purified endogenous lipid molecule. We model the observed cryo-EM density as $PI(3,5)P_2$ on the basis of hATP13A2's robust spermine-dependent ATPase activity and its further potentiation by $PI(3,5)P_2$ (Figures 1A and 1B). What is clear is that this putative $PI(3,5)P_2$ binding site is strategically located to serve as a communication nexus capable of relaying its lipid occupancy status to the transmembrane and cytosolic domains of hATP13A2. More work will be needed to establish the exact mechanism of lipid regulation.

Ion permeation pathway and gating mechanism

The transmembrane domain of the E1-AMPPNP structure occludes a small cavity near the center of the membrane we refer to as the "occlusion chamber" (Figures 3B and S5C). Inside this chamber, the polar sidechains of Tyr259, Tyr940 and Gln944 coordinate the Asp967 carboxyl-sidechain through H-bonds; this tetrad of interacting amino acids is invariant within the P5B-ATPase family (Figures 3B, S1, and S5C). The Asp967 sidechain is likely protonated in the occluded E1-AMPPNP structure since the converse scenario of burying a negatively charged carboxylate-group in the membrane would be energetically prohibitive without a paired counter-charge. We do not know whether counter-transport of protons into the lysosome lumen is involved in the hATP13A2 transport cycle at present. However, the occlusion of Asp967 suggests that it may function as a proton carrier in the E1→E2P transition.

Access to the occlusion chamber from the lysosome lumen is controlled by an ~13 Å hydrophobic barrier formed by M1, M2, M4a and M6 we call the "luminal gate" (Figure 3B). In the E1-

AMPPNP structure the residues Trp251, Tyr256, Tyr259, Thr466, Val467 and Phe963 converge to form a hydrophobic plug "closing" the luminal gate (Figure 3B). In the SPM-E2-BeF_3^- structure the luminal gate "opens" to reveal a narrow "lumen access channel" penetrating 15 Å into the membrane to join the lumen and occlusion chamber (Figures 3B and 3C). The narrow architecture of this access tunnel (~3.2 Å in diameter) departs strikingly from the wide polar funnel (15 to 4 Å in diameter) observed in the E2P structure of SERCA that connects the ER lumen and Ca^{2+} binding sites (Olesen et al., 2007). A comparison of the E1-AMPPNP and SPM-E2-BeF_3^- structures reveals an allosteric mechanism by which autophosphorylation of Asp513, mimicked by BeF_3^- binding, in the P domain opens the luminal gate 59 Å away (Figures 3D–3G and Video S1, refers to Figure 3).

Structural alignment of the SPM-E2-BeF_3^- and SPM-E2-MgF_4^{2-} structures shows that they are very similar andare both in the outward-facing conformation (Figures S3G–S3I, root mean square deviation=0.52 Å). This is in strong contrast to SERCA, which undergoes large conformational changes from an outward-facing state to an occluded state in the E2P→E2-P_i reaction (Olesen et al., 2007). The important implication here is that structural transitions bringing ATP13A from the spermine bound outward-facing state to the next major conformation in the transport cycle must occur after PO_4^{3-} dissociation in the E2-P_i→E1 step (Figure 1C). This next transport cycle intermediate may well be an occluded conformation though its exact nature remains to be determined. These observations underscore the diversity in coupling mechanisms between enzymatic and gating transformations among all P-type ATPases, our understanding of which is still clearly incomplete.

192 **Structural basis of spermine recognition**

193

194 Electrostatic potential surface analysis of the SPM-E2-BeF_3^- structure shows that the lumen access
195 channel possesses a strongly negative charge character, consistent with a possible role in binding
196 positively charged polyamines (Figure 4A). A cigar-shaped cryo-EM density extends from the
197 entrance of the lumen access channel 11 Å down to the occlusion chamber (Figure 4B). Spermine
198 can be easily modelled into this density such that the spermine amine groups come into direct
199 contact with acidic residues in this site (Figure 4C). Therefore, the outer portion of the lumen
200 access channel is the polyamine binding site. In the following discussion we will refer to the four
201 spermine amine groups as N1, N5, N10 and N14, respectively since spermine is a linear chain of
202 14 non-hydrogen atoms (Figures 4D, 4E, and S2E).

203

204 The polyamine binding site overlaps with the luminal gate and occlusion chamber and comprises
205 residues from the external portion of M1, M2, M4a, M5 and M6 (Figures 4B and 4C). Spermine
206 is held in an almost fully extended conformation at the polyamine binding site and is partially
207 dehydrated. N1, N5 and N10 are buried inside the lumen access channel while N14 is exposed to
208 solvent (Figures 4C–4E). For simplicity we will refer to the four sites occupied by N14, N10, N5
209 and N1 as: S0, S1, S2 and S3, respectively (Figure 4C). Since the polyamine binding site is both
210 narrow and embedded halfway inside the electric field of the membrane, the binding of polyamines
211 to hATP13A2 is likely voltage dependent. Based on conservation of 8 of 14 residues in the
212 polyamine binding site (Figure S1), we propose that other members of the P5B-ATPase family are
213 also polyamine transporters. Consistent with this notion, the P5B-ATPase ATP13A3 was found to
214 mediate polyamine transport (Hamouda et al., 2020).

Ion dehydration and selectivity

A fundamental challenge all selective ion transport systems must overcome is the requirement for hydrated ions in solution to be transferred to their binding sites in a completely or partially dehydrated state (Hille, 2001). Ion dehydration incurs significant energetic cost that must be offset by compensating interactions (Gouaux and Mackinnon, 2005). We can understand how hATP13A2 solves the dehydration problem by considering the manner of spermine binding in the polyamine binding site.

The narrow channel architecture of the polyamine binding site constrains N1 to diffuse through S0→S1→S2→S3 in sequence during the spermine binding reaction (Figures 4C–4E). The structure of the polyamine binding site tells us that it is designed to dehydrate polyamine ions in a stepwise fashion: spermine becomes progressively more dehydrated as it migrates deeper into this narrow passage. The significance of this "multistep dehydration" mechanism is that it breaks down the dehydration process into a series of smaller steps with lower kinetic barriers, thus allowing polyamine binding to proceed in a more facile way.

Multistep dehydration can be considered a selectivity mechanism against metal ions; we would expect this effect to favor binding of linear polyamines and not metal ions. hATP13A2 utilizes an additional mechanism of metal ion counter-selection. In selective metal ion channels and transporters, including SERCA, dehydrated metal ions are chelated by a constellation of five to eight oxygen atoms that replaces the inner hydration sphere (Figure S6C) (Gouaux and

Mackinnon, 2005; Sorensen et al., 2004; Toyoshima et al., 2000; Yamashita et al., 2005; Zhou et al., 2001). In hATP13A2, the amine binding sites S1, S2 and S3 can each provide at most two oxygen atoms from carboxylate groups and/or water (Figures 4D–4E). This low coordination number, though apparently sufficient to stabilize dehydrated amine groups in polyamines, is less than that needed to stabilize naked metal ions. Thus, the hATP13A2 polyamine binding site is, by design, not built to handle dehydrated metal ions. We refer to this ion selectivity mechanism as "chelate deprivation".

The origin of spermine selectivity

How can we rationalize hATP13A2's polyamine selectivity profile? Perhaps the most obvious intuition derived from inspecting the polyamine binding site is that hATP13A2 must prefer linear polyamines over cyclic polyamines, as is observed (Figures 1A and S2E). Cyclization constrains the latter to have a minimum cross-section area too large even for the polyamine binding site entrance. Linear polyamines are unconstrained polymer chains and can thus thread through the narrow binding site.

Since putrescine and spermidine are essentially fragments of spermine we can deduce by analogy how they might be docked in the polyamine binding site based on spermine's binding configuration (pose I in Figures 5A and S2E). This analysis predicts that putrescine and spermidine can form two or three ionic interactions with the polyamine binding site, respectively. It follows that hATP13A2's impressive ~100-fold selectivity for spermidine over putrescine (Figure 1A) is explained in part by avidity effects stemming from a greater number of possible ion-pairs formed

by spermidine. Avidity is a selectivity mechanism not available to metal ion transporters. Spermidine binding also buries a larger hydrophobic surface compared to putrescine; thus, stronger spermidine binding is explained additionally by the hydrophobic effect.

hATP13A2 has a more modest ability to discriminate spermine from spermidine (Figure 1A). Binding of spermine and spermidine in the polyamine binding site would involve formation of the same three ion-pairs and buries the same area of hydrophobic surface in our model (Figure 5A). Thus, the contribution of avidity and hydrophobic effects to binding is the same for both spermine and spermidine. How can hATP13A2's ~4-fold spermine preference over spermidine be explained? To understand the origin of hATP13A2's selectivity for spermine we consider the symmetry present in the chemical structure of spermine itself. Spermine and spermidine can enter the polyamine binding site in two possible orientations depicted in Figure 5A as pose I and pose II. What emerges from this picture is that spermine intrinsically has a higher probability of engaging the polyamine binding site in a high affinity configuration compared to spermidine. hATP13A2's apparent preference for spermine over spermidine is thus, at least partly, a reflection of this underlying relationship (Figure 5A).

The selectivity mechanism above presupposes that the polyamine binding site must be sensitive to the degree of spatial matching between amine groups in the bound polyamine molecule and the amine binding sites S1, S2 and S3. The degree of spatial matching can be affected by binding orientation, as discussed above, and also by varying the spacing between amine groups in polyamines. To test the latter, we characterized the effect on ATPase function of a small but focused panel of spermine analogs with varying amine group spacings (Figures 5B–5F). Symmetry

in spermine and its symmetrical analogs restricts hATP13A2 binding to a single possible configuration. We found that norspermine, in which a single methylene (-CH_2-) group from the 4-carbon N5-N10 linker in spermine is removed, exhibits a 10-fold reduction in hATP13A2 binding affinity compared to spermine (Figure 5C and S2E). Further elimination of an additional -CH_2-group from the N5-N10 linker or both N1-N5/N10-N14 linkers from norspermine almost completely abolished hATP13A2 ATPase stimulation in both cases (Figures 5D, 5E and S2E). Thus, the polyamine binding site has evolved to read the length of aliphatic spacers between amine groups in polyamines. The relative positions of S1-S2 and S2-S3 are tuned for recognition of 4-carbon and 3-carbon spacings between amine groups in polyamines, respectively.

The fact that norspermine can potentiate hATP13A2 ATPase function enables us to test the idea that symmetry accounts for spermine's enhanced binding affinity compared to spermidine. If this idea is valid, then one would predict norspermidine to be poorly distinguished from norspermine as both polyamines would make the same interactions with hATP13A2 in all possible orientations due to their inherent symmetry (Figure 5B). This prediction is indeed borne out by our observations (Figures 5C and 5F). Therefore, molecular symmetry is a determinant of polyamine affinity for hATP13A2.

Putative cytosolic ion exit pathway

At the base of the polyamide binding site where it meets the "PPAL" motif in the M4a/b linker the lumen access channel makes a sharp turn and continues toward a side portal between M2 and M6 facing the lipid bilayer (Figures 6A and 6B). The lumen access channel then terminates at a narrow

307 constriction between M2 and M4b formed by Ala472, Ile263 and Ile266 that leads to a funnel-
308 shaped vestibule connected to the cytosol between M1, M2 and M4b (Figures 3C, 6B, and 6C).
309 Ala472, Ile263 and Ile266 likely constitute a "cytosolic gate" since it is the thinnest physical barrier
310 separating the lumen access channel and the cytosolic vestibule in the SPM-E2-BeF_3^- structure
311 (Figure 6C). A chain of ordered solvent molecules connects N1 of the bound spermine molecule
312 and the cytosolic gate, tracing a putative cytosolic ion exit pathway (Figures 6A and 6B).
313
314 **Discussion:**
315
316 P-type metal ion pumps including SERCA and Na^+/K^+-ATPase have internal ion binding sites
317 flanked by gates embedded near the center of the lipid membrane consistent with an alternating
318 access transport mechanism (Drew and Boudker, 2016; Dyla et al., 2020; Jardetzky, 1966). The
319 ATP13A2 polyamine binding site's location in the external portion of the lumen access channel is
320 therefore surprising. Could hATP13A2 residues in positions analogous to Ca^{2+} binding sites in
321 SERCA form an internal binding site that occludes spermine or other polyamines in a subsequent
322 step? This scenario is unlikely, in part because structural alignment of SERCA and hATP13A2
323 transmembrane domains shows that residues involved in Ca^{2+} coordination in SERCA are not
324 conserved in hATP13A2 (Figure S6). We did not find additional cavities in the transmembrane
325 domain that might potentially serve as polyamine occlusion sites.
326
327 Overlap between the luminal gate and polyamine binding site implies that a bound polyamine
328 molecule will act as a wedge preventing closure of the luminal gate. This is incompatible with an
329 alternating access transport mechanism as the latter involves ion occlusion, which cannot happen

330 if the luminal gate is unable to close (Drew and Boudker, 2016; Jardetzky, 1966). The external
331 location of the polyamine binding site, and the single-file arrangement of mobile charges within
332 it, are actually features reminiscent of the selectivity filter of ion channels (Zhou et al., 2001). The
333 selectivity filter is the narrowest part of an ion conducting pore optimized for selectivity and
334 throughput (Gouaux and Mackinnon, 2005; Hille, 2001). We propose that hATP13A2 may sample
335 an ion channel-like intermediate state — a "pump-channel" in which both the luminal gate and
336 cytosolic gate are open following PO_4^{3-} release from the polyamine bound E2-P_i state (Figure 7).
337 In this intermediate state the polyamine binding site acts as a selectivity filter to enforce selective
338 ion movement across the membrane. This mechanism could explain selective polyamine transport
339 by hATP13A2 without invoking the existence of an ion occlusion chamber. We know at least one
340 other P-type pump that can function as an ion channel: the palytoxin-modified Na^+/K^+-ATPase
341 pump-channel described by Artigas and Gadsby (Artigas and Gadsby, 2002). Perhaps ATP13A2
342 evolved to exploit an ion channel-like state during its transport cycle, independent of toxin binding.
343 This pump-channel model should bear consideration because it suggests the tantalizing possibility
344 that hATP13A2 may act as a spermine/spermidine conduit to depolarize the lysosome and thus
345 promote V-type ATPase driven proton flux (Mindell, 2012). Such a function could account for the
346 impaired lysosome acidification observed in the settings of Parkinson's disease-linked ATP13A2
347 mutations and targeted ATP13A2 knock-out (Dehay et al., 2012b; van Veen et al., 2020). The
348 results presented here offer fertile ground to understand more deeply the mechanisms and
349 implications of ATP13A2-mediated transport and regulation in the context of lysosome function
350 and neurodegeneration.
351

The new ATP13A2 structures permit a confident mapping of disease mutations onto two distinct conformational states in the transport cycle of ATP13A2 (Figure S7). Mutations associated with hereditary spastic paraplegia and neuronal ceroid lipofuscinosis are concentrated near the catalytic site in the P-domain and likely impact ATP binding and/or autophosphorylation. The remaining mutations associated with Kufor-Rakeb syndrome and early-onset Parkinson's disease are distributed throughout the ATP13A2 structure and possibly affect the folding, maturation and/or stability of the protein. The precise explanations as to why particular mutations are associated with a specific disease phenotype will require additional study. Notably, disease-associated loss-of-function mutations are conspicuously absent from the polyamine binding site and the ion permeation pathway. The underlying reasons for this curious pattern are unclear and may warrant further investigation. However, the ATP13A2 structures described here provide a firm foundation to begin rationalizing ATP13A2 mutations associated with neurodegenerative disorders.

In summary, this work describes cryo-EM structures of the Parkinson's disease linked polyamine transporter ATP13A2 in occluded and spermine-bound states. Comparison of these structures reveal the ion permeation pathway and gating mechanism. Our structural and functional analysis establishes the physical principles of selective polyamine transport. These principles are relevant to any mechanistic consideration of other polyamine transport systems found in animals, bacteria, fungi and plants since the problem of transporting linear organic polycations across membranes is fundamentally the same in all organisms (Fujita et al., 2012; Igarashi and Kashiwagi, 1999). The surprising location of the polyamine binding site and its implications for the transport mechanism highlights the P-type ATPase fold as an impressively malleable platform for catalyzing the movement of polar substances across membranes. Structures and mechanisms presented here

provide useful counterpoints to understand the operation of all P-type ATPases transporting disparate materials including metal ions, protons, lipids and peptides (Abe et al., 2018; Huang et al., 2017; McKenna et al., 2020; Morth et al., 2007; Olesen et al., 2007; Pedersen et al., 2007; Shinoda et al., 2009; Toyoshima et al., 2000).

Conclusion:

Our findings refine the current knowledge of ion transport mechanisms among P-type ATPases. The structures described here furnish rich opportunities for pharmacological investigation of ATP13A2s's therapeutic potential in disease contexts including cancer and Parkinson's disease (Madeo et al., 2018).

Acknowledgments: We thank Mohamed Trebak, Christopher Yengo, Lisa Shantz and Donald Gill for critical reading of the manuscript and Chen Xu for help with SerialEM. This work was supported by The Pennsylvania State University start-up funds to K.L.

Author contributions: J.T. and D.B. performed protein expression, purification and biochemistry experiments. D.B. performed the molecular biology experiments. K.L performed EM experiments. K.L. conceived and supervised the project. J.T. and K.L. analyzed the results. K.L. wrote the manuscript.

397 **Competing interests:** Authors declare that they have no competing interests.

398

399 **Data and materials availability:** Cryo-EM density maps of the hATP13A2 E1-AMPPNP, SPM-
400 E2-BeF_3^- and SPM-E2-MgF_4^{2-} forms have been deposited in the electron microscopy data bank
401 under accession code EMD-23683, EMD-23684 and EMD-23685, respectively. Atomic
402 coordinates of the hATP13A2 E1-AMPPNP, SPM-E2-BeF_3^- and SPM-E2-MgF_4^{2-} have been
403 deposited in the protein data bank under accession code 7M5V, 7M5X and 7M5Y, respectively.
404 Materials are available from the corresponding author upon reasonable request.

405

406 **References:**

407

408 Abe, K., Irie, K., Nakanishi, H., Suzuki, H., and Fujiyoshi, Y. (2018). Crystal structures of the
409 gastric proton pump. Nature *556*, 214-218, 10.1038/s41586-018-0003-8.

410 Adams, P.D., Afonine, P.V., Bunkoczi, G., Chen, V.B., Davis, I.W., Echols, N., Headd, J.J.,
411 Hung, L.W., Kapral, G.J., Grosse-Kunstleve, R.W.*, et al.* (2010). PHENIX: a comprehensive
412 Python-based system for macromolecular structure solution. Acta Crystallogr D Biol Crystallogr
413 *66*, 213-221, 10.1107/S0907444909052925.

414 Albers, R.W. (1967). Biochemical aspects of active transport. Annu Rev Biochem *36*, 727-756,
415 10.1146/annurev.bi.36.070167.003455.

416 Artigas, P., and Gadsby, D.C. (2002). Ion channel-like properties of the Na+/K+ Pump. Ann N Y
417 Acad Sci *976*, 31-40, 10.1111/j.1749-6632.2002.tb04711.x.

418 Bergeron, R.J., McManis, J.S., Weimar, W.R., Schreier, K.M., Gao, F., Wu, Q., Ortiz-Ocasio, J.,
419 Luchetta, G.R., Porter, C., and Vinson, J.R. (1995). The role of charge in polyamine analogue
420 recognition. J Med Chem *38*, 2278-2285, 10.1021/jm00013a003.

421 Bras, J., Verloes, A., Schneider, S.A., Mole, S.E., and Guerreiro, R.J. (2012). Mutation of the
422 parkinsonism gene ATP13A2 causes neuronal ceroid-lipofuscinosis. Hum Mol Genet *21*, 2646-
423 2650, 10.1093/hmg/dds089.

424 Chen, V.B., Arendall, W.B., 3rd, Headd, J.J., Keedy, D.A., Immormino, R.M., Kapral, G.J.,
425 Murray, L.W., Richardson, J.S., and Richardson, D.C. (2010). MolProbity: all-atom structure

validation for macromolecular crystallography. Acta Crystallogr D Biol Crystallogr *66*, 12-21, 10.1107/S0907444909042073.

Cheng, A., Eng, E.T., Alink, L., Rice, W.J., Jordan, K.D., Kim, L.Y., Potter, C.S., and Carragher, B. (2018). High resolution single particle cryo-electron microscopy using beam-image shift. J Struct Biol *204*, 270-275, 10.1016/j.jsb.2018.07.015.

Clarkson, A.N., Liu, H., Pearson, L., Kapoor, M., Harrison, J.C., Sammut, I.A., Jackson, D.M., and Appleton, I. (2004). Neuroprotective effects of spermine following hypoxic-ischemic-induced brain damage: a mechanistic study. FASEB J *18*, 1114-1116, 10.1096/fj.03-1203fje.

Dehay, B., Martinez-Vicente, M., Ramirez, A., Perier, C., Klein, C., Vila, M., and Bezard, E. (2012a). Lysosomal dysfunction in Parkinson disease: ATP13A2 gets into the groove. Autophagy *8*, 1389-1391, 10.4161/auto.21011.

Dehay, B., Ramirez, A., Martinez-Vicente, M., Perier, C., Canron, M.H., Doudnikoff, E., Vital, A., Vila, M., Klein, C., and Bezard, E. (2012b). Loss of P-type ATPase ATP13A2/PARK9 function induces general lysosomal deficiency and leads to Parkinson disease neurodegeneration. Proc Natl Acad Sci U S A *109*, 9611-9616, 10.1073/pnas.1112368109.

Di Fonzo, A., Chien, H.F., Socal, M., Giraudo, S., Tassorelli, C., Iliceto, G., Fabbrini, G., Marconi, R., Fincati, E., Abbruzzese, G.*, et al.* (2007). ATP13A2 missense mutations in juvenile parkinsonism and young onset Parkinson disease. Neurology *68*, 1557-1562, 10.1212/01.wnl.0000260963.08711.08.

Drew, D., and Boudker, O. (2016). Shared Molecular Mechanisms of Membrane Transporters. Annu Rev Biochem *85*, 543-572, 10.1146/annurev-biochem-060815-014520.

447 Dykstra, W.G., Jr., and Herbst, E.J. (1965). Spermidine in Regenerating Liver: Relation to Rapid
448 Synthesis of Ribonucleic Acid. Science *149*, 428-429, 10.1126/science.149.3682.428.

449 Dyla, M., Kjaergaard, M., Poulsen, H., and Nissen, P. (2020). Structure and Mechanism of P-
450 Type ATPase Ion Pumps. Annu Rev Biochem *89*, 583-603, 10.1146/annurev-biochem-010611-
451 112801.

452 Emsley, P., Lohkamp, B., Scott, W.G., and Cowtan, K. (2010). Features and development of
453 Coot. Acta Crystallogr D Biol Crystallogr *66*, 486-501, 10.1107/S0907444910007493.

454 Estrada-Cuzcano, A., Martin, S., Chamova, T., Synofzik, M., Timmann, D., Holemans, T.,
455 Andreeva, A., Reichbauer, J., De Rycke, R., Chang, D.I.*, et al.* (2017). Loss-of-function
456 mutations in the ATP13A2/PARK9 gene cause complicated hereditary spastic paraplegia
457 (SPG78). Brain *140*, 287-305, 10.1093/brain/aww307.

458 Fujita, M., Fujita, Y., Iuchi, S., Yamada, K., Kobayashi, Y., Urano, K., Kobayashi, M.,
459 Yamaguchi-Shinozaki, K., and Shinozaki, K. (2012). Natural variation in a polyamine
460 transporter determines paraquat tolerance in Arabidopsis. Proc Natl Acad Sci U S A *109*, 6343-
461 6347, 10.1073/pnas.1121406109.

462 Goddard, T.D., Huang, C.C., Meng, E.C., Pettersen, E.F., Couch, G.S., Morris, J.H., and Ferrin,
463 T.E. (2018). UCSF ChimeraX: Meeting modern challenges in visualization and analysis. Protein
464 Sci *27*, 14-25, 10.1002/pro.3235.

465 Goehring, A., Lee, C.H., Wang, K.H., Michel, J.C., Claxton, D.P., Baconguis, I., Althoff, T.,
466 Fischer, S., Garcia, K.C., and Gouaux, E. (2014). Screening and large-scale expression of

membrane proteins in mammalian cells for structural studies. Nat Protoc *9*, 2574-2585, 10.1038/nprot.2014.173.

Gouaux, E., and Mackinnon, R. (2005). Principles of selective ion transport in channels and pumps. Science *310*, 1461-1465, 10.1126/science.1113666.

Hamouda, N.N., Van den Haute, C., Vanhoutte, R., Sannerud, R., Azfar, M., Mayer, R., Cortes Calabuig, A., Swinnen, J.V., Agostinis, P., Baekelandt, V.*, et al.* (2020). ATP13A3 is a major component of the enigmatic mammalian polyamine transport system. J Biol Chem, 10.1074/jbc.RA120.013908.

Heymann, J.B., and Belnap, D.M. (2007). Bsoft: image processing and molecular modeling for electron microscopy. J Struct Biol *157*, 3-18, 10.1016/j.jsb.2006.06.006.

Hille, B. (2001). Ion channels of excitable membranes, 3rd edn (Sunderland, Mass.: Sinauer).

Ho, B.K., and Gruswitz, F. (2008). HOLLOW: generating accurate representations of channel and interior surfaces in molecular structures. BMC Struct Biol *8*, 49, 10.1186/1472-6807-8-49.

Holemans, T., Sorensen, D.M., van Veen, S., Martin, S., Hermans, D., Kemmer, G.C., Van den Haute, C., Baekelandt, V., Gunther Pomorski, T., Agostinis, P.*, et al.* (2015). A lipid switch unlocks Parkinson's disease-associated ATP13A2. Proc Natl Acad Sci U S A *112*, 9040-9045, 10.1073/pnas.1508220112.

Huang, C.S., Pedersen, B.P., and Stokes, D.L. (2017). Crystal structure of the potassium-importing KdpFABC membrane complex. Nature *546*, 681-685, 10.1038/nature22970.

Igarashi, K., and Kashiwagi, K. (1999). Polyamine transport in bacteria and yeast. Biochem J *344 Pt 3*, 633-642.

Jardetzky, O. (1966). Simple allosteric model for membrane pumps. Nature *211*, 969-970, 10.1038/211969a0.

Kimanius, D., Forsberg, B.O., Scheres, S.H., and Lindahl, E. (2016). Accelerated cryo-EM structure determination with parallelisation using GPUs in RELION-2. Elife *5*, 10.7554/eLife.18722.

Klein, C., and Westenberger, A. (2012). Genetics of Parkinson's disease. Cold Spring Harb Perspect Med *2*, a008888, 10.1101/cshperspect.a008888.

Lee, K.P.K., Chen, J., and MacKinnon, R. (2017). Molecular structure of human KATP in complex with ATP and ADP. Elife *6*, 10.7554/eLife.32481.

Lin, C.H., Tan, E.K., Chen, M.L., Tan, L.C., Lim, H.Q., Chen, G.S., and Wu, R.M. (2008). Novel ATP13A2 variant associated with Parkinson disease in Taiwan and Singapore. Neurology *71*, 1727-1732, 10.1212/01.wnl.0000335167.72412.68.

Madeo, F., Eisenberg, T., Pietrocola, F., and Kroemer, G. (2018). Spermidine in health and disease. Science *359*, 10.1126/science.aan2788.

Mastronarde, D.N. (2003). SerialEM: A Program for Automated Tilt Series Acquisition on Tecnai Microscopes Using Prediction of Specimen Position. Microscopy and Microanalysis *9*, 1182–1183.

505 McKenna, M.J., Sim, S.I., Ordureau, A., Wei, L., Harper, J.W., Shao, S., and Park, E. (2020).
506 The endoplasmic reticulum P5A-ATPase is a transmembrane helix dislocase. Science *369*,
507 10.1126/science.abc5809.

508 Michael, A.J. (2016). Polyamines in Eukaryotes, Bacteria, and Archaea. J Biol Chem *291*,
509 14896-14903, 10.1074/jbc.R116.734780.

510 Mindell, J.A. (2012). Lysosomal acidification mechanisms. Annu Rev Physiol *74*, 69-86,
511 10.1146/annurev-physiol-012110-142317.

512 Morth, J.P., Pedersen, B.P., Buch-Pedersen, M.J., Andersen, J.P., Vilsen, B., Palmgren, M.G.,
513 and Nissen, P. (2011). A structural overview of the plasma membrane Na+,K+-ATPase and H+-
514 ATPase ion pumps. Nat Rev Mol Cell Biol *12*, 60-70, 10.1038/nrm3031.

515 Morth, J.P., Pedersen, B.P., Toustrup-Jensen, M.S., Sorensen, T.L., Petersen, J., Andersen, J.P.,
516 Vilsen, B., and Nissen, P. (2007). Crystal structure of the sodium-potassium pump. Nature *450*,
517 1043-1049, 10.1038/nature06419.

518 Olesen, C., Picard, M., Winther, A.M., Gyrup, C., Morth, J.P., Oxvig, C., Moller, J.V., and
519 Nissen, P. (2007). The structural basis of calcium transport by the calcium pump. Nature *450*,
520 1036-1042, 10.1038/nature06418.

521 Palmgren, M.G., and Nissen, P. (2011). P-type ATPases. Annu Rev Biophys *40*, 243-266,
522 10.1146/annurev.biophys.093008.131331.

523 Park, J.S., Blair, N.F., and Sue, C.M. (2015). The role of ATP13A2 in Parkinson's disease:
524 Clinical phenotypes and molecular mechanisms. Mov Disord *30*, 770-779, 10.1002/mds.26243.

525 Pedersen, B.P., Buch-Pedersen, M.J., Morth, J.P., Palmgren, M.G., and Nissen, P. (2007).
526 Crystal structure of the plasma membrane proton pump. Nature *450*, 1111-1114,
527 10.1038/nature06417.

528 Pegg, A.E. (2016). Functions of Polyamines in Mammals. J Biol Chem *291*, 14904-14912,
529 10.1074/jbc.R116.731661.

530 Pettersen, E.F., Goddard, T.D., Huang, C.C., Couch, G.S., Greenblatt, D.M., Meng, E.C., and
531 Ferrin, T.E. (2004). UCSF Chimera--a visualization system for exploratory research and
532 analysis. J Comput Chem *25*, 1605-1612, 10.1002/jcc.20084.

533 Post, R.L., Kume, S., Tobin, T., Orcutt, B., and Sen, A.K. (1969). Flexibility of an active center
534 in sodium-plus-potassium adenosine triphosphatase. J Gen Physiol *54*, 306-326,
535 10.1085/jgp.54.1.306.

536 Punjani, A., Rubinstein, J.L., Fleet, D.J., and Brubaker, M.A. (2017). cryoSPARC: algorithms
537 for rapid unsupervised cryo-EM structure determination. Nat Methods *14*, 290-296,
538 10.1038/nmeth.4169.

539 Punjani, A., Zhang, H., and Fleet, D.J. (2020). Non-uniform refinement: adaptive regularization
540 improves single-particle cryo-EM reconstruction. Nat Methods *17*, 1214-1221, 10.1038/s41592-
541 020-00990-8.

542 Ramirez, A., Heimbach, A., Grundemann, J., Stiller, B., Hampshire, D., Cid, L.P., Goebel, I.,
543 Mubaidin, A.F., Wriekat, A.L., Roeper, J.*, et al.* (2006). Hereditary parkinsonism with dementia
544 is caused by mutations in ATP13A2, encoding a lysosomal type 5 P-type ATPase. Nat Genet *38*,
545 1184-1191, 10.1038/ng1884.

546 Rohou, A., and Grigorieff, N. (2015). CTFFIND4: Fast and accurate defocus estimation from
547 electron micrographs. J Struct Biol *192*, 216-221, 10.1016/j.jsb.2015.08.008.

548 Scharschmidt, B.F., Keeffe, E.B., Blankenship, N.M., and Ockner, R.K. (1979). Validation of a
549 recording spectrophotometric method for measurement of membrane-associated Mg- and NaK-
550 ATPase activity. J Lab Clin Med *93*, 790-799.

551 Scheres, S.H. (2012). RELION: implementation of a Bayesian approach to cryo-EM structure
552 determination. J Struct Biol *180*, 519-530, 10.1016/j.jsb.2012.09.006.

553 Scheres, S.H. (2016). Processing of Structurally Heterogeneous Cryo-EM Data in RELION.
554 Methods Enzymol *579*, 125-157, 10.1016/bs.mie.2016.04.012.

555 Schorb, M., Haberbosch, I., Hagen, W.J.H., Schwab, Y., and Mastronarde, D.N. (2019).
556 Software tools for automated transmission electron microscopy. Nat Methods *16*, 471-477,
557 10.1038/s41592-019-0396-9.

558 Schultheis, P.J., Hagen, T.T., O'Toole, K.K., Tachibana, A., Burke, C.R., McGill, D.L.,
559 Okunade, G.W., and Shull, G.E. (2004). Characterization of the P5 subfamily of P-type transport
560 ATPases in mice. Biochem Biophys Res Commun *323*, 731-738, 10.1016/j.bbrc.2004.08.156.

561 Sehnal, D., Svobodova Varekova, R., Berka, K., Pravda, L., Navratilova, V., Banas, P., Ionescu,
562 C.M., Otyepka, M., and Koca, J. (2013). MOLE 2.0: advanced approach for analysis of
563 biomacromolecular channels. J Cheminform *5*, 39, 10.1186/1758-2946-5-39.

564 Shinoda, T., Ogawa, H., Cornelius, F., and Toyoshima, C. (2009). Crystal structure of the
565 sodium-potassium pump at 2.4 A resolution. Nature *459*, 446-450, 10.1038/nature07939.

566 Sorensen, D.M., Holemans, T., van Veen, S., Martin, S., Arslan, T., Haagendahl, I.W., Holen,
567 H.W., Hamouda, N.N., Eggermont, J., Palmgren, M., *et al.* (2018). Parkinson disease related
568 ATP13A2 evolved early in animal evolution. PLoS One *13*, e0193228,
569 10.1371/journal.pone.0193228.

570 Sorensen, T.L., Moller, J.V., and Nissen, P. (2004). Phosphoryl transfer and calcium ion
571 occlusion in the calcium pump. Science *304*, 1672-1675, 10.1126/science.1099366.

572 Spataro, R., Kousi, M., Farhan, S.M.K., Willer, J.R., Ross, J.P., Dion, P.A., Rouleau, G.A., Daly,
573 M.J., Neale, B.M., La Bella, V., *et al.* (2019). Mutations in ATP13A2 (PARK9) are associated
574 with an amyotrophic lateral sclerosis-like phenotype, implicating this locus in further phenotypic
575 expansion. Hum Genomics *13*, 19, 10.1186/s40246-019-0203-9.

576 Stein, N. (2008). CHAINSAW: a program for mutating PDB files used as templates in molecular
577 replacement. J Appl Crystallogr *41*, 641–643.

578 Toyoshima, C., Nakasako, M., Nomura, H., and Ogawa, H. (2000). Crystal structure of the
579 calcium pump of sarcoplasmic reticulum at 2.6 A resolution. Nature *405*, 647-655,
580 10.1038/35015017.

581 van Veen, S., Martin, S., Van den Haute, C., Benoy, V., Lyons, J., Vanhoutte, R., Kahler, J.P.,
582 Decuypere, J.P., Gelders, G., Lambie, E., *et al.* (2020). ATP13A2 deficiency disrupts lysosomal
583 polyamine export. Nature *578*, 419-424, 10.1038/s41586-020-1968-7.

584 Vrijsen, S., Besora-Casals, L., van Veen, S., Zielich, J., Van den Haute, C., Hamouda, N.N.,
585 Fischer, C., Ghesquiere, B., Tournev, I., Agostinis, P., *et al.* (2020). ATP13A2-mediated endo-

586 lysosomal polyamine export counters mitochondrial oxidative stress. Proc Natl Acad Sci U S A
587 *117*, 31198-31207, 10.1073/pnas.1922342117.

588 Yamashita, A., Singh, S.K., Kawate, T., Jin, Y., and Gouaux, E. (2005). Crystal structure of a
589 bacterial homologue of Na+/Cl--dependent neurotransmitter transporters. Nature *437*, 215-223,
590 10.1038/nature03978.

591 Yang, Y., Chen, S., Zhang, Y., Lin, X., Song, Y., Xue, Z., Qian, H., Wang, S., Wan, G., Zheng,
592 X.*, et al.* (2017). Induction of autophagy by spermidine is neuroprotective via inhibition of
593 caspase 3-mediated Beclin 1 cleavage. Cell Death Dis *8*, e2738, 10.1038/cddis.2017.161.

594 Zheng, S.Q., Palovcak, E., Armache, J.P., Verba, K.A., Cheng, Y., and Agard, D.A. (2017).
595 MotionCor2: anisotropic correction of beam-induced motion for improved cryo-electron
596 microscopy. Nat Methods *14*, 331-332, 10.1038/nmeth.4193.

597 Zhou, Y., Morais-Cabral, J.H., Kaufman, A., and MacKinnon, R. (2001). Chemistry of ion
598 coordination and hydration revealed by a K+ channel-Fab complex at 2.0 A resolution. Nature
599 *414*, 43-48, 10.1038/35102009.

600 Zivanov, J., Nakane, T., Forsberg, B.O., Kimanius, D., Hagen, W.J., Lindahl, E., and Scheres,
601 S.H. (2018). New tools for automated high-resolution cryo-EM structure determination in
602 RELION-3. Elife *7*, 10.7554/eLife.42166.

603

604

Methods:

Cell lines

Sf9 cells were cultured in Sf-900 II SFM medium (GIBCO) at 28°C. HEK293S GnTI$^-$ cells cultured in Freestyle 293 medium (GIBCO) supplemented with 2% FBS at 37°C. Cell lines were acquired from and authenticated by American Type Culture Collection (ATCC). The cell lines were not tested for mycoplasma contamination.

Protein expression and purification

cDNA encoding full-length human ATP13A2 isoform A (hATP13A2, UniProt ID Q9NQ11-1) was cloned into the pEG BacMam vector containing a C-terminal GFP preceded by a PreScission protease cleavage site (Goehring et al., 2014). hATP13A2 was expressed in HEK293S GnTI$^-$ cells using the BacMam method. In brief, bacmids encoding the hATP13A2-GFP fusion were generated using DH10Bac cells according to the manufacturer's instructions. BacMam baculoviruses were produced using *Spodoptera frugiperda* Sf9 cells cultured in SF900II SFM medium. For protein expression, suspension cultures of HEK293S GnTI$^-$ cells cultured in Freestyle 293 medium were infected with BacMam baculovirus at a density of ~1.5x10^6 cells/ml. After 24 hrs at 37°C, the infected cultures were supplemented with 10 mM sodium butyrate and grown for a further 24 hrs at 30°C before harvesting. All subsequent manipulations were performed at 4°C.

For large-scale purification, cell pellets from 4 liters of culture were resuspended in lysis buffer containing 50mM Hepes, pH 7.5, 150mM NaCl, 2mM DTT and supplemented with a protease inhibitors cocktail (Lee et al., 2017). The cell suspension was disrupted in a Dounce homogenizer and the resulting lysate was clarified at 39800 x g for 30 min. The crude membrane pellet obtained was then resuspended once again in lysis buffer and was stirred for 2 hrs in the presence of 1.5% (w/v) lauryl maltose neopentyl glycol (LMNG) and 0.3% (w/v) cholesteryl hemisuccinate (CHS). The solubilized membranes were clarified by centrifugation at 39800 x g for 45 min and the resulting supernatant was mixed with GFP nanobody-coupled sepharose resin (prepared in-house) by rotation. After 60 min, the resin was collected and washed with 20 column volumes of wash buffer containing 20 mM Hepes, pH 7.5, 150mM NaCl, 1 mM DTT, 0.03% (w/v) dodecylmaltoside (DDM) and 0.0015% (w/v) cholesteryl hemisuccinate (CHS). PreScission protease was used to elute hATP13A2 from the GFP nanobody resin by overnight incubation. The eluted protein was concentrated to a volume of ~500 uL prior to fractionation on a Superose 6 column equilibrated with 20 mM Hepes, pH 7.5, 150mM NaCl, 1 mM DTT, 0.03% (w/v) DDM and 0.0015% (w/v) CHS. Peak fractions were collected and concentrated to their final target concentrations before imaging by cryo-EM.

ATPase activity assay

An NADH-coupled fluorimetric assay was used to measure ATPase activity (Scharschmidt et al., 1979). Mg^{2+}-ATP was added to a mixture containing 0.046 to 0.092 μM hATP13A2, 50 mM Hepes, pH 7.5, 150 mM KCl, 30 mM $MgCl_2$, 60 μg/mL pyruvate kinase, 32 μg/mL lactate dehydrogenase, 4 mM phosphoenolpyruvate, and 300 μM NADH. Consumption of NADH was

650 measured by monitoring the fluorescence at λ_{ex}=340 nm and λ_{em}=445 nm using a SpectraMax
651 Gemini microplate reader (Molecular Devices). Rates of ATP hydrolysis were calculated by
652 converting fluorescence loss to nmol NADH per minute using known standards of NADH. Data
653 were then fit by nonlinear regression to the Michaelis-Menten equation to calculate K_M and V_{max}
654 values using GraphPad Prism. In lipid dependence experiments DPPA or PA were each
655 supplemented at 0.1 mg/mL. Inhibition experiments were performed with the additional
656 supplementation of: 1) 3 mM AMPPNP; 2) 5 mM $MgCl_2$ and 10 mM NaF; or 3) 2 mM $BeSO_4$ and
657 10 mM NaF.
658
659 EM data acquisition
660
661 Purified hATP13A2 was concentrated to ~5.0 mg/mL and supplemented with the following
662 additives: i) 5.0 mM $MgCl_2$, 2.0 mM AMPPNP; ii) 0.1 mM spermine, 5.0 mM $MgCl_2$, 2.0 mM
663 $BeSO_4$, 10.0 mM NaF; or iii) 0.1 mM spermine, 5.0 mM $MgCl_2$, 10.0 mM NaF. The supplemented
664 protein sample was incubated at room temperature for ~3 hrs and passed through a 0.45 µm filter
665 to remove debris. To prepare cryo-EM grids, 3.5 µL drops of supplemented and filtered
666 hATP13A2 were applied to Quantifoil R1.2/1.3 400 mesh Au grids glow-discharged for 60 sec.
667 The grids were blotted for 4 sec at 4°C and 100% humidity before being plunge-frozen in liquid
668 ethane using a Vitrobot Mark IV (FEI). The grids were imaged using a Titan Krios G3 transmission
669 electron microscope (FEI) operated at 300 kV and a Gatan BioQuantum energy filter slit width of
670 5 eV. Automated data collection was performed with SerialEM using the beam-image shift method
671 (Cheng et al., 2018; Mastronarde, 2003; Schorb et al., 2019). A Gatan K3 Summit direct electron
672 detector was used to record movies in super-resolution counting mode with a super-resolution

673 pixel size of 0.415 Å. Movies were recorded for 3.0 to 3.5 s over 60 or 70 frames using a dose-rate
674 of 15 electrons per pixel per second with a defocus range of 0.6 to 1.8 μm or 0.5 to 1.3 μm. The
675 total cumulative doses were 60 to 76 electrons per $Å^2$ (1.09 electrons per $Å^2$ per frame).
676
677 Image processing and map calculation
678
679 The same data processing strategy was used in the early stages of structure determination to obtain
680 all three hATP13A2 3D reconstructions presented in this study (Figure S4A). Briefly, dose-
681 fractionated super-resolution movies were 2x2 down-sampled by Fourier cropping to a final pixel
682 size of 0.83 Å. The down-sampled movie frames were used for grid-based motion correction and
683 dose-filtering with MotionCor2 (Zheng et al., 2017). CTF parameters were estimated from the
684 corrected movie frames using CTFFIND4.1 (Rohou and Grigorieff, 2015). The entire dataset was
685 then inspected to eliminate micrographs exhibiting imaging defects including excessive drift,
686 cracked ice or defocus values exceeding the specified range. Micrographs with estimated CTF
687 resolution worse than 5 Å were discarded. The remaining motion-corrected dose-filtered movie
688 sums were subjected to automated particle picking in RELION3.1 using a Laplacian-of-Gaussian
689 filter to obtain an initial particle set (Kimanius et al., 2016; Scheres, 2012, 2016; Zivanov et al.,
690 2018). Particle images extracted from the motion-corrected dose-filtered micrographs as 384x384
691 pixel boxes were down-sampled to 96x96 pixel particle stacks in RELION. Iterative 2D
692 classification in RELION using down-sampled particle stacks was performed to remove spurious
693 images of ice, carbon support and other debris.
694

For the E1-AMPPNP dataset, 740,626 particles from the best 2D classes were re-extracted without down-sampling as 384x384 pixel boxes in RELION (Figure S4B). *Ab initio* 3D classification was performed in cryoSPARC (Punjani et al., 2017) with C1 symmetry (Figure S4A). The *ab initio* models obtained were used as initial models for heterogeneous refinement resulting in one "good" class with clear protein features. The remaining "junk" classes were uninterpretable. 515,611 particles corresponding to the "good" class were subjected to a round of homogeneous refinement, resulting in a 3.43 Å reconstruction. Non-uniform refinement was performed using the refined 3D model to obtain a 3.00 Å reconstruction (Punjani et al., 2020). Lastly, local refinement was performed using a mask that includes the micelle density, which resulted in a final reconstruction at FSC=0.143 resolution of 2.9 Å (Figure S4E). Local resolution estimates mapped onto the final 3D reconstruction is shown in Figure S4H.

For the SPM-E2-BeF_3^- dataset, the data processing strategy used was similar to that of the E1-AMPPNP dataset. Briefly, 1,368,235 particles from the best 2D classes were re-extracted without down-sampling as 384x384 pixel boxes in RELION (Figure S4C). *Ab initio* 3D classification was performed in cryoSPARC v2 with C1 symmetry to obtain three *de novo* classes (Figure S4A). The *ab initio* models obtained were used as initial models for of heterogeneous refinement resulting in one good class with clear protein features. The "good" class was then submitted to a round of non-uniform refinement. The refined particles were then used for a second round of heterogeneous refinement with the non-uniform refined model and "junk" models from the previous round of heterogeneous refinement as starting models. The resulting "junk" particles were eliminated, and the remaining "good" particles were subjected to another around of non-uniform refinement. The process of heterogeneous refinement and non-uniform refinement was iterated until the resolution

718 of the non-uniform refined model no longer improves. The final round of non-uniform refinement
719 using 648,247 particles yielded a refined 3D model at 3.13 A resolution. Lastly, local refinement
720 was performed using a mask that includes detergent micelle density, resulting in a final
721 reconstruction at FSC=0.143 resolution of 2.7 Å (Figure S4F). Local resolution estimates mapped
722 onto the final 3D reconstruction is shown in Figure S4I.
723
724 For the SPM-E2-MgF_4^{2-} dataset, a data processing strategy similar to that used for the SPM-E2-
725 BeF_3^- dataset was applied. Briefly, 466,778 particles from the best 2D classes were re-extracted
726 without down-sampling as 384x384 pixel boxes in RELION (Figure S4D). *Ab initio* 3D
727 classification was performed in cryoSPARC v2 with C1 symmetry to obtain three *de novo* classes.
728 Iterative heterogeneous refinement and non-uniform refinement was then performed as described
729 for the SPM-E2-BeF_3^- dataset. The final round of non-uniform refinement using 285,797 particles
730 resulted in a refined 3D model at 3.22 A resolution. Lastly, local refinement was performed using
731 a mask that includes detergent micelle density, resulting in a final reconstruction at FSC=0.143
732 resolution of 3.0 Å (Figure S4G). Local resolution estimates mapped onto the final 3D
733 reconstruction is shown in Figure S4J.
734
735 Model building and coordinate refinement
736
737 Model building was initially performed in the E1-AMPPNP map. The crystal structure of rabbit
738 skeletal muscle SERCA (PDB: 3N8G) was used as a reference structure to generate the starting
739 model for building hATP13A2. Briefly, the SERCA model was first mutated generate a
740 polyalanine model using CHAINSAW (Stein, 2008) and manually divided into its transmembrane

741 domain and individual cytosolic domains. The domains were then docked into EM density
742 separately by rigid-body fitting using the fitmap function in UCSF Chimera (Pettersen et al., 2004)
743 followed by manual rebuilding in Coot (Emsley et al., 2010). The EM density was of sufficient
744 quality to allow manual rebuilding in Coot. B-factor sharpening was performed locally in Coot
745 "on-the-fly" to optimize observable map features for model building. The membrane embedded
746 region of the NTD and the CTD were manually built *de novo* in Coot. The β-sandwich structure
747 in the NTD was built using the N-terminal extension of the cryo-EM structure of yeast P5A-
748 ATPase Spf (PDB: 6XMQ) as a starting model. The NTD exhibits a lower local resolution
749 compared to the rest of the reconstruction and is built partly as a polyalanine model (a.a. 45 to 86).
750 Rotamers were modeled for residues with poor sidechain density in the rest of the structure.
751 Automatic real space refinement of the model against a half map was performed using
752 `phenix.real_space_refine` (Adams et al., 2010). Tight secondary structure and geometric
753 restraints were used to minimize overfitting. Manual rebuilding in Coot was alternated with
754 automated refinement in `phenix.real_space_refine`. A similar strategy was used to build
755 the SPM-E2-BeF_3^- and SPM-E2-MgF_4^{2-} structures, except the refined E1-AMPPNP coordinates
756 was used as the starting model.
757
758 FSC curves were calculated between refined models and the half-map used for refinement
759 (FSC_{work}) or the half-map kept for cross-validation (FSC_{free}) (Figure S4K to M). Model quality
760 was evaluated by MolProbity (Chen et al., 2010) (Table S1).
761
762 Local resolution was estimated using `blocres` with a box size of 20 (Heymann and Belnap,
763 2007). The occlusion chamber and lumen access channel were identified using HOLLOW (Ho and

764 Gruswitz, 2008) and MOLE 2.5 (Sehnal et al., 2013). All structure figures were generated using

765 UCSF ChimeraX (Goddard et al., 2018).

766 **Figure legends:**

767

768 **Figure 1. Architecture of human ATP13A2.** (A) Polyamine-dependent ATPase activity of
769 hATP13A2. Purified hATP13A2 exhibits dose-dependent polyamine stimulated ATPase activity
770 characterized by apparent Michaelis constants: SPM ($K_{M,SPM}$=26.4 μM), SPD ($K_{M,SPD}$=118.3 μM).
771 Putrescine and the cyclic polyamine 1,4,8,11-tetraazacyclotetradecane (cyclam) did not
772 appreciably stimulate hATP13A2 ATPase activity and are assumed to have a K_M>10 mM. 1 mM
773 ATP was used in the reactions. Data points represent mean ± SEM (n=3). SPM – spermine, SPD
774 – spermidine, PUT – putrescine. (B) Lipid dependence of hATP13A2 ATPase activity. ATPase
775 activity of hATP13A2 in the presence of 1 mM SPM and 370 μM ATP with lipid supplementation.
776 DPPA - dipalmitoylphosphatidic acid, PI(3,5)P_2 – dipalmitoyl-phosphatidylinositol-3,5-
777 bisphosphate. Data points represent mean ± SEM (n=3, ****P<0.0001). One-way ANOVA
778 analysis was performed. (C) The reaction cycle of ATP13A2. Polyamine import takes place during
779 the E2P to E1 half-cycle. Compounds used for stabilizing reaction intermediates are colored in
780 red. PA – polyamine, P_i – inorganic phosphate. (D) Topology diagram of hATP13A2.
781 Transmembrane helices M1 to M10 are numbered. TM – transmembrane domain, A – actuator
782 domain, P – phosphorylation domain, N – nucleotide binding domain, NTD – N-terminal extension
783 domain, CTD – C-terminal extension domain. The same domain abbreviations are used in all
784 figures. (E) Cryo-EM density map of the E1-AMPPNP structure. (F) Ribbons representation of
785 the atomic model of the E1-AMPPNP structure. The NTD contains a distinctive triangular "spade-
786 like" structure containing three helices penetrating the inner-leaflet of the membrane (see also
787 Figures S5A and S5B). This "spade" is cemented to the A domain via a β-sandwich structure. The

788 CTD is composed by a linker that connects the end of M10 to an α-helix (αCTD) docked onto the
789 surface of the P domain via hydrophobic contacts. Coloring as in (D).
790
791 **Figure 2. Function of ATP13A2 extensions.** (A) Comparison of hATP13A2 and SERCA
792 structures. The hATP13A2 E1-AMPPNP and SERCA E1-AMPPCP (PDB ID 3N8G) structures
793 were aligned over their M7-M10 supporting domains and shown as grey and black α-carbon traces,
794 respectively. A domains and the attached M1-M2 segments of hATP13A2 and SERCA are colored
795 red and green, respectively. The hATP13A2 NTD is colored purple. Sideview (left - superposition)
796 and top views (top-right – hATP13A2 and bottom-right – SERCA) are shown. Catalytic glutamate
797 in the TGES motif and phosphorylated aspartate residues in the P domain are indicated by solid
798 circles. The NTD lowers the energy barrier toward formation of the "outward-open" E2P
799 conformation by bringing the A domain closer to its destination in the reaction coordinate. Cyto.
800 – cytosol. (B) Putative PI(3,5)P_2 binding site. Electrostatic potential surface of the hATP13A2 E1-
801 AMPPNP structure (left - sideview). Close-up view of the putative PI(3,5)P_2 binding site (boxed
802 region on the left) shown in ribbons presentation (right). Sidechains are shown in ball-and-stick
803 representation. Cryo-EM density corresponding to the modelled PI(3,5)P_2 is shown as a blue mesh.
804 Coloring as in Figure 1F.
805
806 **Figure 3. Gating mechanism of the lumen access channel.** (A) Cryo-EM map of the SPM-E2-
807 $BeF3^-$ structure. Coloring as in Figure 1D. (B) The occlusion chamber. Cartoon representation of
808 the E1-AMPPNP structure with helices shown as cylinders. M1-M2, M4a-M4b, and M5-M6 are
809 colored green, red and blue, respectively. Sidechains of residues corresponding to the luminal gate,
810 occlusion chamber and hinge are colored gray, white and orange, respectively. The volume

811 enclosed by the occlusion chamber is shown as a yellow surface. Conformational changes
812 associated with autophosphorylation and ADP dissociation are indicated by arrows. Polar and
813 hydrophobic residues from M1, M2, M5 and M6 line the walls of the occlusion chamber and the
814 conserved “PPAL” motif in the M4a/b linker forms the base. The luminal gate is "closed” in the
815 E1-AMPPNP structure. (C) The lumen access channel. Cartoon representation of the SPM-E2-
816 BeF_3^- structure with helices shown as cylinders. The lumen access channel is shown as a yellow
817 surface. Coloring as in (B). Contact between the base of M1 and top of M4b is maintained during
818 the coupled movement of M1 and M2 through the interaction between Tyr240 and Pro474, which
819 serves as a hinge for the motion. The displacement of M1 and M2 induced by autophosphorylation
820 and ADP dissociation enables the aromatic sidechains of residues Trp251, Tyr256 and Tyr259 to
821 rotate away from Thr466, Val467 and Phe963; this dissolves the hydrophobic plug and “opens”
822 the luminal gate, revealing the lumen access channel. (D to G) Conformational changes coupled
823 to autophosphorylation and ADP dissociation. E1-AMPPNP and SPM-E2-BeF_3^- structures were
824 aligned over their M7-M10 supporting domains and shown as red and blue α-carbon traces,
825 respectively. Arrows are used to indicate direction of motion. (D) The A domain swings forward
826 to displace the N domain from the P domain following Asp513 phosphorylation and ADP release.
827 The trajectory of the A domain’s swing is constrained by its association with the NTD whose
828 “spade” acts as a pivot for this motion. (E) The A domain and the P domain also rotate toward
829 each other, bringing the TGES motif near Asp513 to catalyze dephosphorylation of the latter in a
830 subsequent step. (F) Rotation of the P domain moves its P1 helix up toward the membrane and
831 exerting a force on the cytosolic end of M4b. This causes the M4a-M4b segment to buckle at the
832 M4a/b linker. (G) The swinging motion of the A domain exerts a pull on M1 and M2 through

833 direct attachments resulting in the rotation and downward translation of these transmembrane
834 segments toward the cytosol.
835
836 **Figure 4. Structural basis of spermine recognition.** (A) Electrostatic potential surface of the
837 lumen access channel entrance viewed from the lumen. (B) Location of the polyamine binding
838 site. The transmembrane domain of hATP13A2 is shown in ribbons representation. Coloring of
839 helices as in Figure 3C. Topview (left) is in the same perspective as in (A). Sideview is shown on
840 the right. Cryo-EM density of the bound spermine molecule is colored yellow. (C) Architecture of
841 the polyamine binding site. Close-up view of the polyamine binding site (left). Spermine and
842 residues lining the polyamine binding site are colored yellow and gray, respectively and shown in
843 ball-and-stick representation. Helices colored as in (B). Cryo-EM densities of the bound spermine
844 and solvent are shown as transparent surfaces colored yellow and purple, respectively. Water is
845 shown as red spheres. Amine group binding sites S0 to S3 are indicated by brackets (right). Some
846 polyamine binding site residues are omitted in the right panel for clarity. (D and E) Interactions
847 between spermine amine groups and the polyamine binding site. Topviews of S0 to S3 are shown.
848 Coloring as in (C). Transparent van der Waals surfaces of sidechains and solvent molecules in S0
849 to S3 are shown in (E). His255 and Pro1039 make up S0 and do not come into close contact with
850 N14. As a result, N14 is less ordered and is free to interact with solvent molecules. In S1, N10
851 interacts directly with Asp960 through coulombic interactions while a water molecule associated
852 with Asn957 and an Asp254-Arg460 salt-bridge surround N10 in a polar environment. The
853 chemical environment of S2 is very different from S1 and is the narrowest part of the polyamine
854 binding site (diameter≈3.2 Å, Figure 6C). In S2, a completely dehydrated N5 interacts with both
855 oxygen atoms of the Asp463 sidechain carboxyl group while Trp251, Tyr256 and Phe963 encircle

N5 on three sides with aromatic sidechains. In S3, N1 interacts tightly with Asp967 and is further surrounded by a combination of polar and hydrophobic residues: Trp251, Tyr259, Thr466, Val467 and Gln944. Additionally, N1 interacts with a water molecule kept just below S3.

Figure 5. Origin of spermine selectivity. (A) Model of polyamine binding to hATP13A2. Amine and aliphatic groups are shown as blue circles and black sticks, respectively. Amine binding sites S1 to S3 are drawn as square brackets. Spermine, spermidine and putrescine can enter the polyamine binding site in two possible orientations (Pose I and II). Suboptimal interactions are indicated by asterisks. Spermine bound in pose I and pose II are chemically indistinguishable configurations due to its symmetry. In pose II spermidine makes what must be a weaker interaction with the polyamine binding site compared to pose I as only two of three possible ion-pairs can be formed. Putrescine can adopt both poses shown in any orientation. (B) Spermine and spermidine analogs used for structure activity relationship analysis. A shorthand denoting the length of aliphatic linkers between amine groups is used. 3-3-3 – norspermine, 3-2-3 – 1,2-Bis(3-aminopropylamino)ethane, 2-3-2 – N,N′-Bis(2-aminoethyl)-1,3-propanediamine, 3-3 – norspermidine. (C to F) Dose-response curves showing the effect of spermine and spermidine analogs shown in (B) on hATP13A2 ATPase activity in the presence of 1 mM ATP. Apparent Michaelis constants: norspermine ($K_{M,3\text{-}3\text{-}3}$=267.0 μM), norspermidine ($K_{M,3\text{-}3}$=394.5 μM). 3-2-3 and 2-3-2 did not appreciably stimulate ATPase activity. Abbreviations as in (B). Results from the spermine titration in Figure 1A shown as a reference. Error bars represent mean ± SEM (n=3).

Figure 6. A putative cytosolic ion exit pathway. (A-B) A detailed view of the cytosolic gate region in the SPM-E2-BeF_3^- structure is shown. The tunnel beneath the polyamine binding site

879 leads to a narrow constriction referred to in the text as the "cytosolic gate" formed by Ile263,
880 Ile266 and Ala472. On the other side of the cytosolic gate is a funnel-shaped "cytosolic vestibule"
881 that leads to the cytoplasm. Ordered solvent molecules are shown as red spheres. Cryo-EM density
882 corresponding to solvent is shown as transparent purple surfaces in (A). The lumen access channel
883 and the cytosolic vestibule are rendered as transparent yellow surfaces in (B). Helices are colored
884 as in Figure 3C. (C) Tunnel radius along the ion pathway. A plot of the tunnel radius of the lumen
885 access channel and cytosolic vestibule estimated using MOLE 2.5 is shown. The locations of the
886 polyamine binding site, cytosolic gate and cytosolic vestibule are indicated.
887
888 **Figure 7. Proposed mechanism of polyamine transport.** Since Asp967 is likely uncharged when
889 it is occluded, we suggest that it obtains a proton from the cytosol during the E1→E1-ATP step.
890 Autophosphorylation and ADP release precedes the E2P state, at which point polyamine and/or
891 proton exchange with the lysosomal lumen takes place. Binding of spermine or spermidine
892 stimulates ATP13A2 dephosphorylation. Release of PO_4^{3-} from the ATPase active site triggers
893 formation of a "pump-channel" intermediate, in which both luminal and cytosolic gates are open,
894 thus allowing polyamine translocation into the cytosol. Binding of $PI(3,5)P_2$ or PA to the $PI(3,5)P_2$
895 binding site potentiates the transport cycle.
896
897

898 **Supplementary Figure Legends:**

899

900 **Figure S1. Sequence alignment of P5B-ATPases, related to Figures 1, 2, 3, 4, 5, 6, and 7.** A
901 multiple sequence alignment of human P-type ATPases belonging to the P5B family. The protein
902 sequence of rabbit SERCA and pig Na^+/K^+-ATPase are also included in the alignment. Sequence
903 alignment was performed using ClustalW and adjusted manually. Shading in the sequence
904 alignment indicate degree of conservation. Green arrows and red bars indicate β-strands and α-
905 helices, respectively. Polyamine binding sites residues are highlighted by green boxes. Ca^{2+}
906 binding site residues in SERCA are indicated by red boxes. The conserved TGES motif and the
907 autophosphorylated aspartate residue are colored purple. The PPAL motif in the M4a/b-linker is
908 indicated by gray shading.

909

910 **Figure S2. Purification and characterization of hATP13A2, related to Figure 1.** (A) Size-
911 exclusion chromatography (SEC) profile of affinity purified hATP13A2. Asterisk indicates
912 fractions analyzed by SDS-PAGE. (B) Coomassie stained SDS-PAGE gel of SEC purified
913 hATP13A2. Asterisk indicates fractions in (A) there were analyzed. Predicted $MW_{hATP13A2}$≈128.8
914 kDa. (C) Spermine-dependent ATPase activity of hATP13A2. ATPase activity was measured
915 using purified hATP13A2 at 6 μg/mL in the presence or absence of 100 μM spermine. Data points
916 represent mean ± SEM (n=3). The apparent $K_{M,ATP}$ is 0.946 mM. (D) hATP13A2 ATPase activity
917 in the presence of inhibitors. hATP13A2 is sensitive to inhibition by the phosphomimetics MgF_4^{2-},
918 BeF_3^- or and the ATP analog AMPPNP. ATPase inhibition assays were performed in the presence
919 of 10 μM spermine and 370 μM ATP. Data points represent mean ± SEM (n=3, ***P<0.001).

One-way ANOVA analysis was performed. (E) Chemical structures of spermine, spermidine, putrescine and cyclam.

Figure S3. Comparison of hATP13A2 structures, related to Figures 1, 2, and 7. (A to C) Zoomed in views of the ATPase active site in the E1-AMPPNP, SPM-E2-BeF_3^- structure and SPM-E2-MgF_4^{2-} structures, respectively. Coloring as in Figure 1D. Residues involved in autophosphorylation and dephosphorylation of Asp531 are shown. Cryo-EM densities corresponding to Mg^{2+}-AMPPNP, Mg^{2+}-BeF_3^- and Mg^{2+}-MgF_4^{2-} are shown as green meshes. (D to F) α-carbon traces of the E1-AMPPNP (green), SPM-E2-BeF_3^- (blue) and SPM-E2-MgF_4^{2-} (red) structures, respectively. (G to I) Pairwise superpositions of hATP13A2 structures. Coloring as in D to F. (G) E1-AMPPNP vs SPM-E2-MgF_4^{2-}. (H) E1-AMPPNP vs SPM-E2-BeF_3^-. (I) SPM-E2-BeF_3^- vs SPM-E2-MgF_4^{2-}.

Figure S4. Image processing and resolution estimates, related to Figures 1, 2, 3, and 4. (A) Outline of data processing strategy used for all datasets. (B to D) Representative 2D classes from the three datasets: E1-AMPPNP (B), SPM-E2-BeF_3^- (C) and SPM-E2-MgF_4^{2-} (D). (E to M) Estimates of global and local resolutions of the 3D reconstructions and the cross-validation of atomic models. (E, H and K) E1-AMPPNP structure. (F, I and L) SPM-E2-BeF_3^- structure. (G, J and M) SPM-E2-MgF_4^{2-} structure. (E to G) FSC curves calculated between independently refined half maps. (H to J) Local resolution maps. (K to M) Cross-validation FSC curves of the model vs. full map (FSC_{full}), model vs. half map used for structure refinement (FSC_{work}) and model vs half map excluded from structure refinement (FSC_{free}).

Figure S5. The lipid embedded NTD and the occlusion chamber in the E1-AMPPNP structure, related to Figures 2, and 3. (A) The micelle density of the E1-AMPPNP structure. Cryo-EM density corresponding to the detergent micelle is low-pass filtered to 20 Å and shown along with the atomic-model of the E1-AMPPNP structure displayed in cartoon representation. The NTD is colored purple. The "spade" portion of the NTD is embedded in what can be considered the "inner leaflet" of the detergent micelle. (B) Lipid bilayer organization surrounding hATP13A2. Here lipid or detergent molecules bound to the periphery of hATP13A2's transmembrane domain are shown in orange to delineate the lipid bilayer environment close to the protein. Cryo-EM density of the E1-AMPPNP structure is shown in gray. The insertion of the NTD in the inner leaflet can be readily appreciated. (C) Detailed view of the occlusion chamber in the E1-AMPPNP structure. Sidechains lining the occlusion chamber in the E1-AMPPNP structure are shown in ball-and-stick representation and colored in gray. Water molecules are shown as red spheres. Helices are colored as in Figure 3B. Cryo-EM density corresponding to occluded solvent is shown as transparent purple surfaces.

Figure S6. Comparison of SERCA and hATP13A2 structures, related to Figure, related to Figures 3, 4, and 7. (A to D) Sidechains involved in Ca^{2+} coordination and proton binding in SERCA and the analogous residues in hATP13A2 are shown in ball-and-stick representation and colored gray. Ca^{2+} ions are shown as green spheres. Spermine is shown in ball-and-stick representation and colored yellow. Structures were aligned over M7 to M10. (A) hATP13A2 E1-AMPPNP. (B) hATP13A2 SPM-E2-BeF_3^-. (C) SERCA Ca^{2+}-E1-AMPPCP (PDB ID 3N8G). (D) SERCA H^+-E2-BeF_3^- (PDB ID 3B9B)

966 **Figure S7. Disease-associated mutations in human ATP13A2, related to Figure 7.** (A and B)
967 Mapping of ATP13A2 residues mutated in human diseases to hATP13A2 structures presented in
968 this study. Gray α-carbon traces of hATP13A2 models are shown. α-carbon atoms of mutated
969 residues are rendered as colored spheres according to the indicated coloring scheme. (A)
970 hATP13A2 E1-AMPPNP. (B) hATP13A2 SPM-E2-BeF_3^-. PD – Early-onset Parkinson's disease,
971 KRS – Kufor-Rakeb syndrome, HSP – hereditary spastic paraplegia, NCL – neuronal ceroid
972 lipofuscinosis.

973

974 **Video S1. Allosteric mechanism for gating the lumen access channel**

975

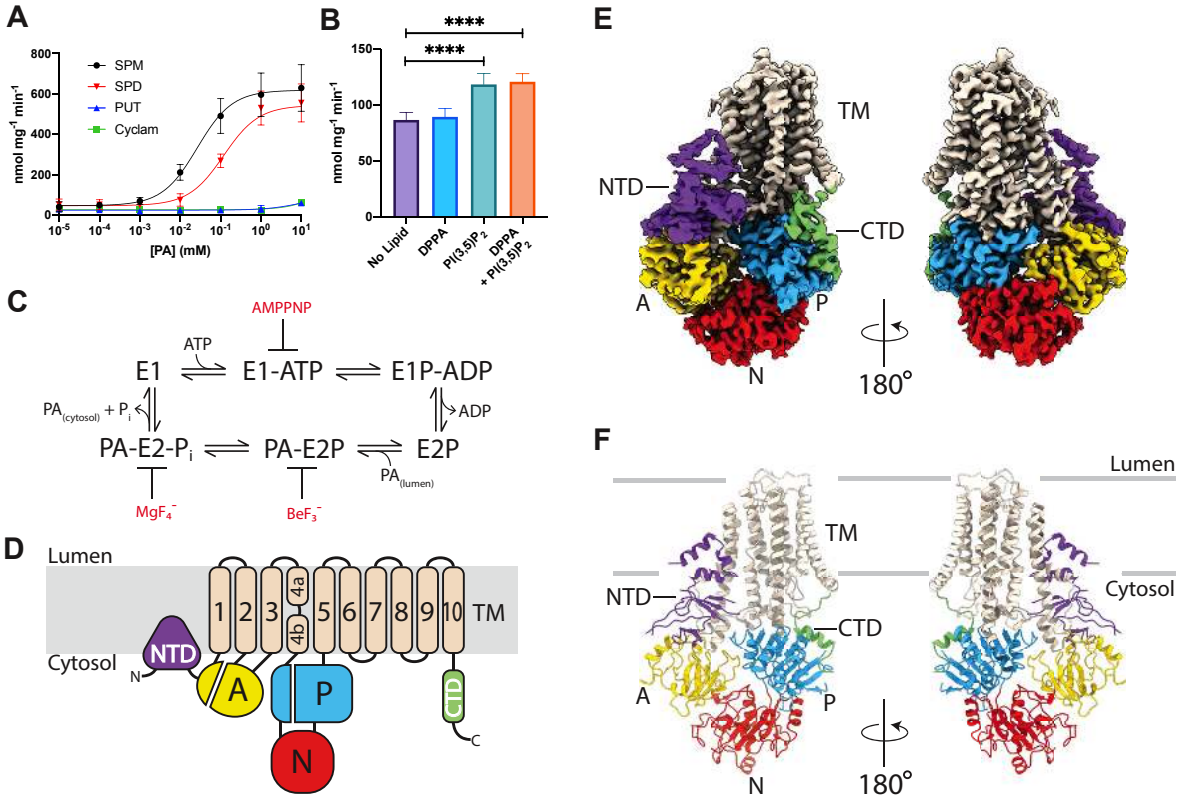

Figure 1. Architecture of human ATP13A2.

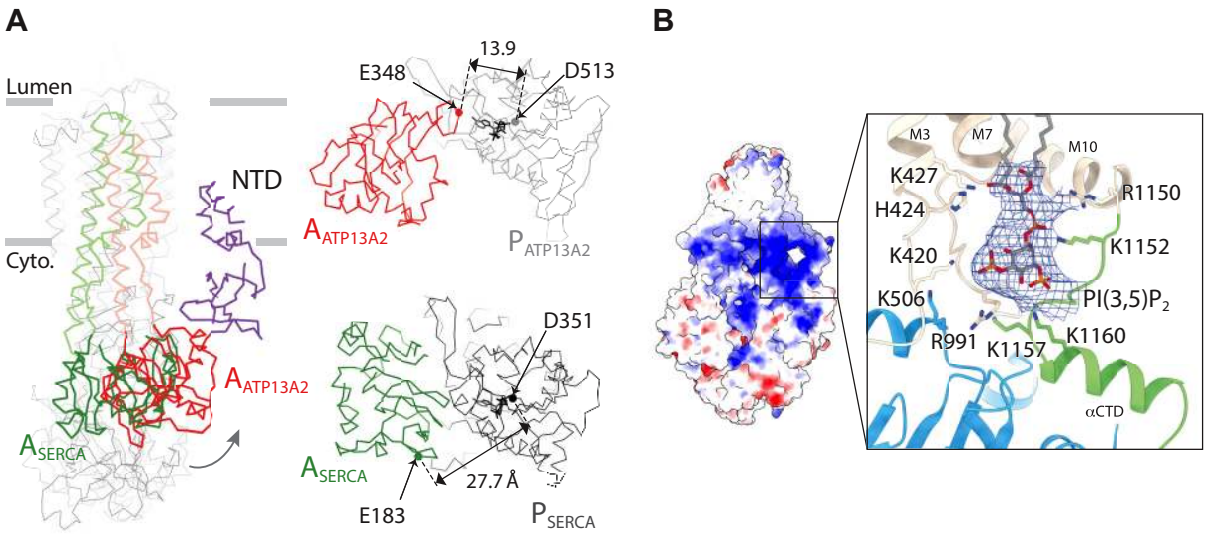

Figure 2. Function of ATP13A2 extensions.

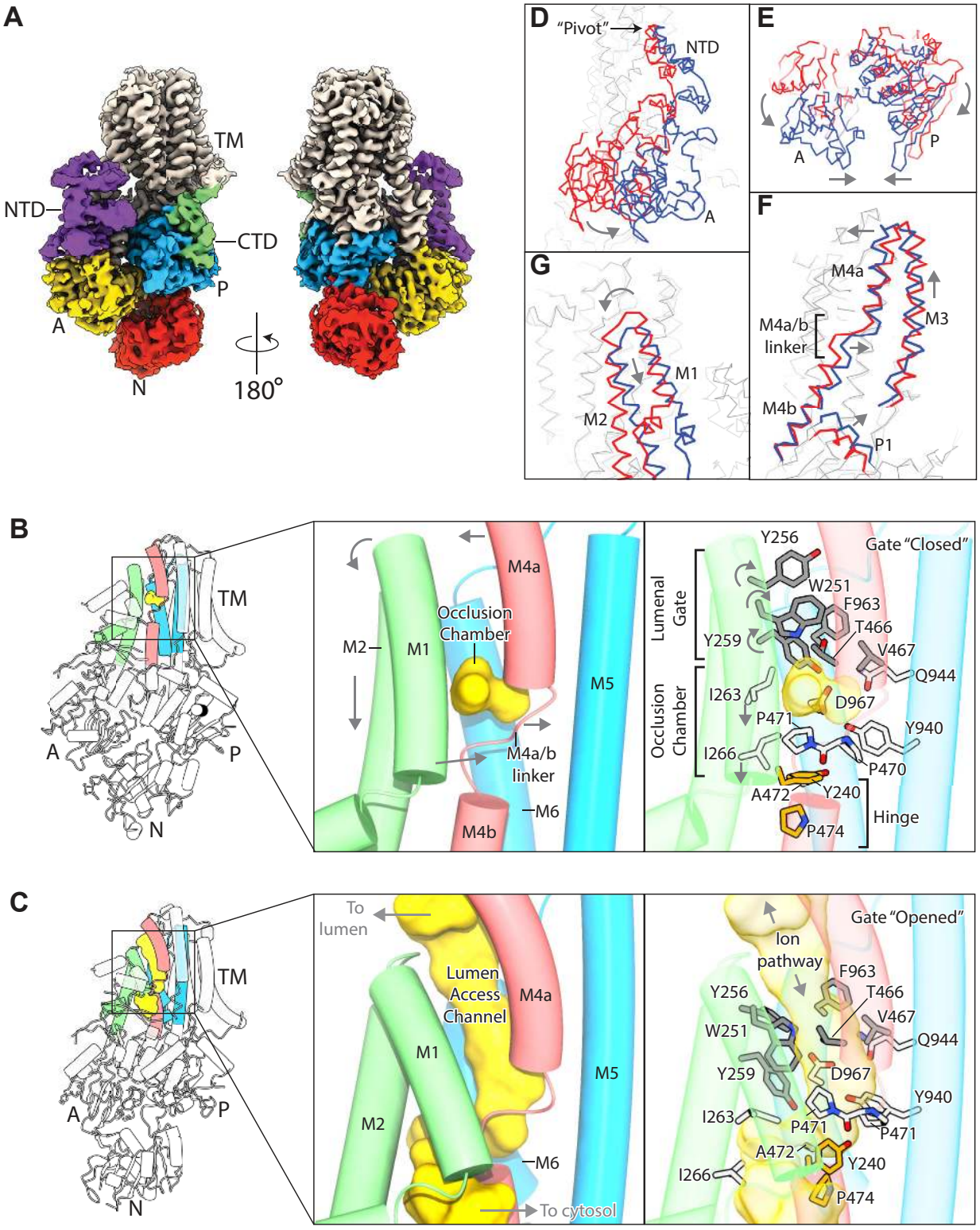

Figure 3. Gating mechanism of the lumen access channel.

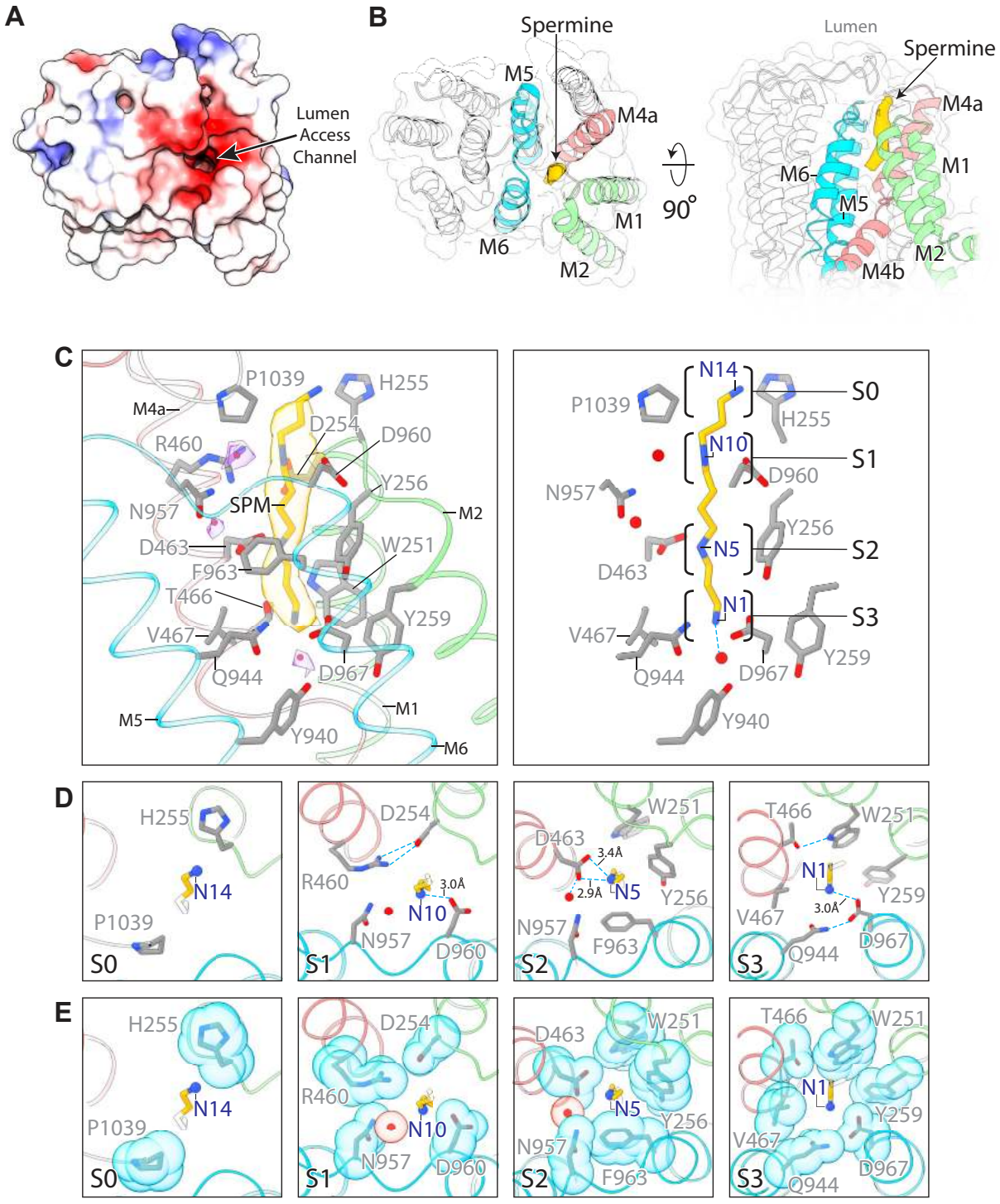

Figure 4. Structural basis of spermine recognition.

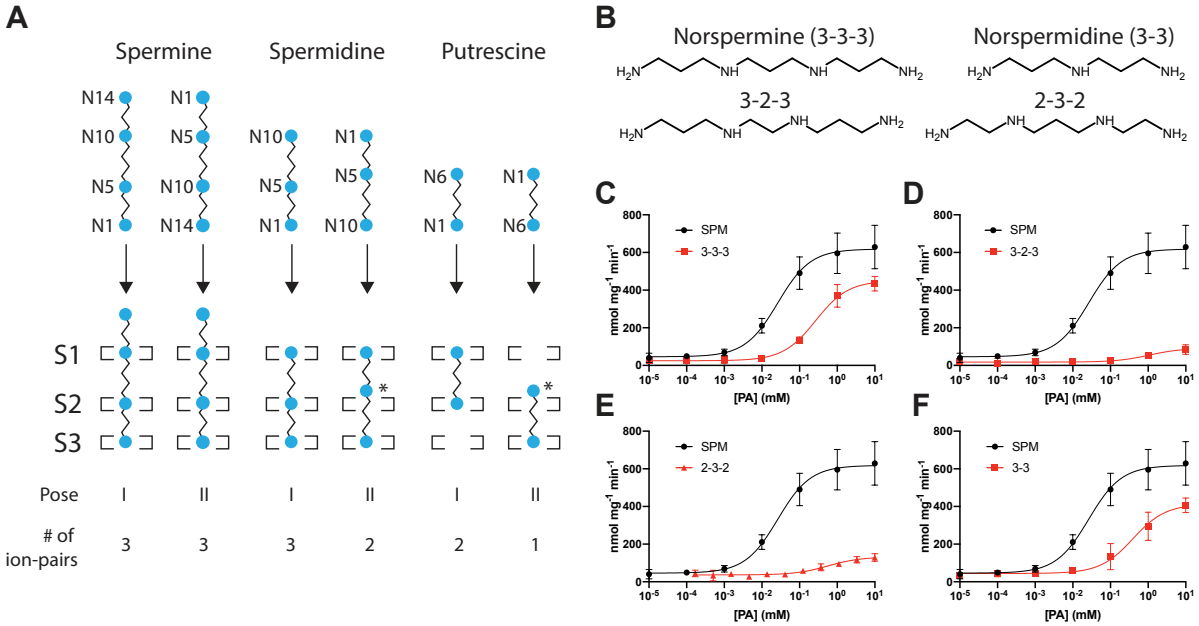

Figure 5. Origin of spermine selectivity.

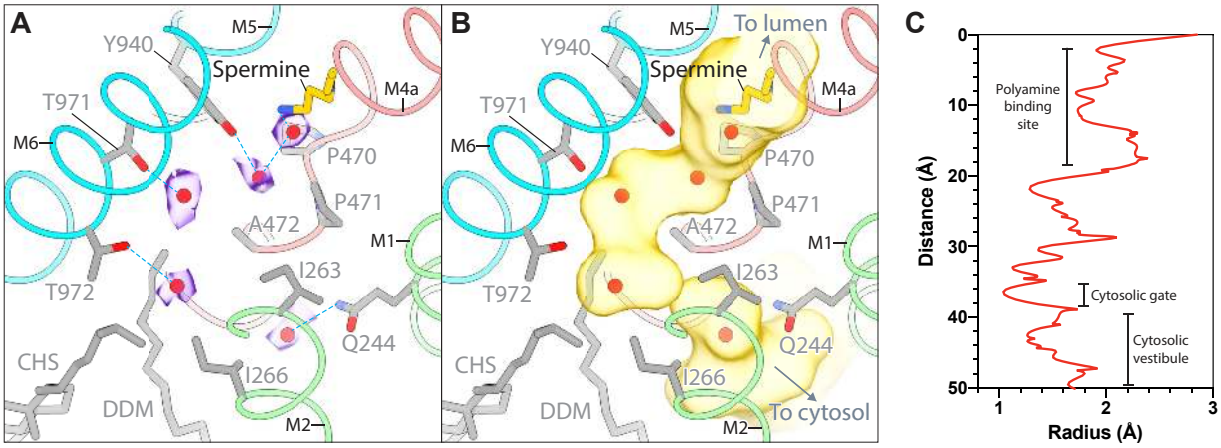

Figure 6. A putative cytosolic ion exit pathway.

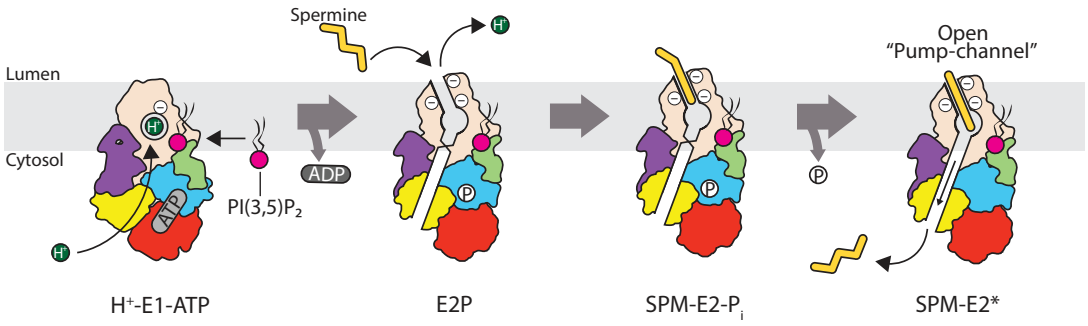

Figure 7. Proposed mechanism of polyamine transport.

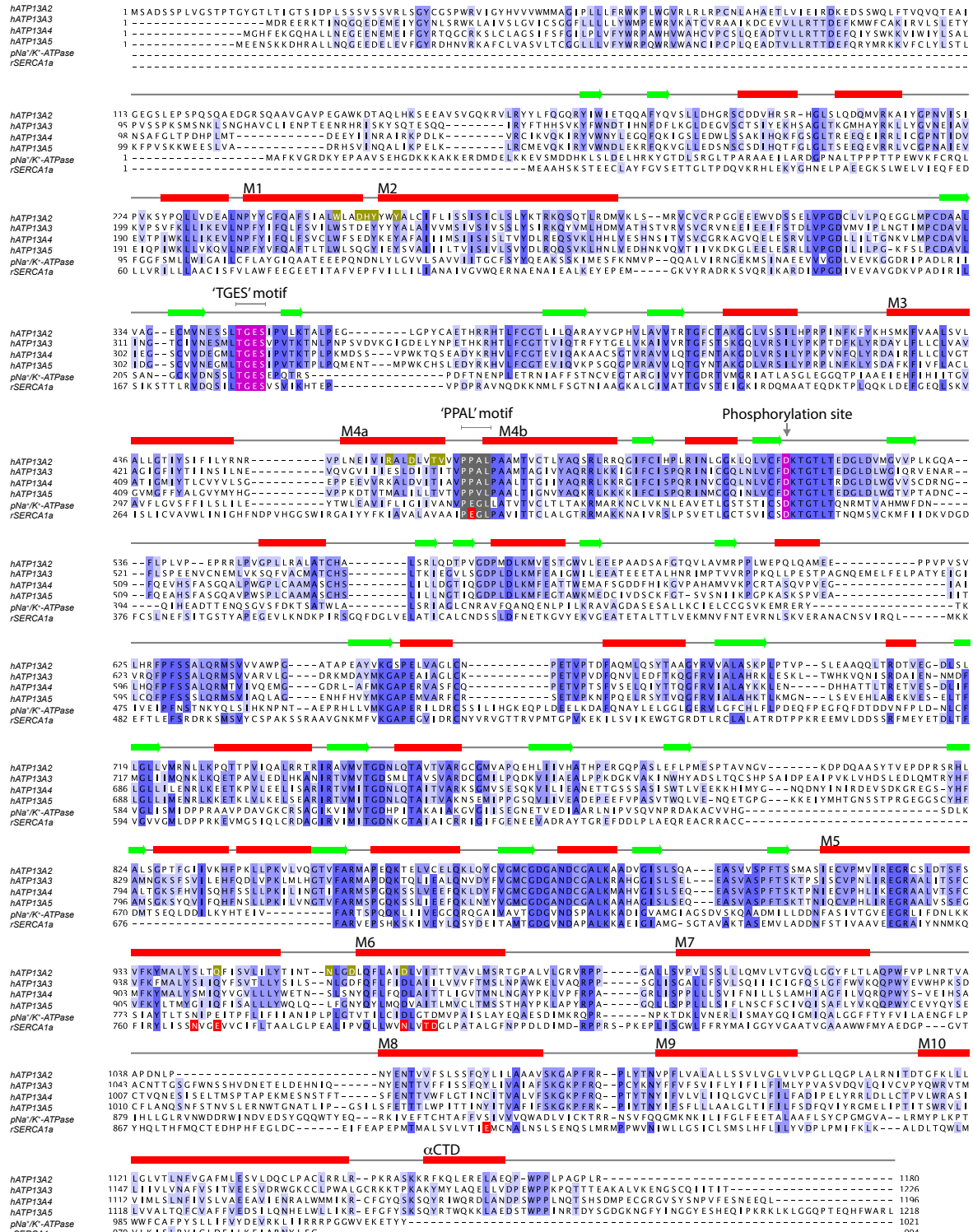

Figure S1. Sequence alignment of P5B-ATPases, related to Figures 1, 2, 3, 4, 5, 6, and 7.

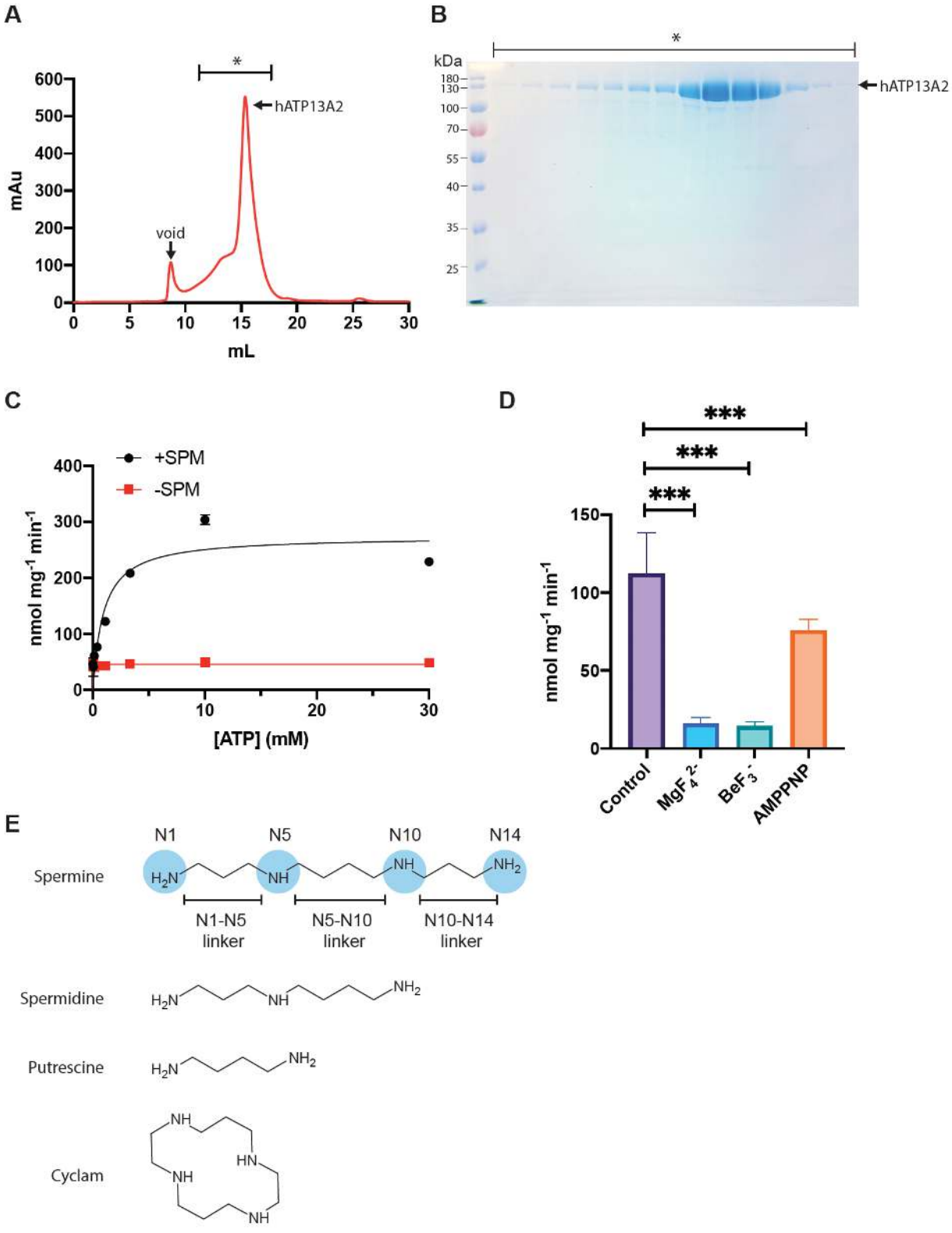

Figure S2. Purification and characterization of hATP13A2, related to Figure 1.

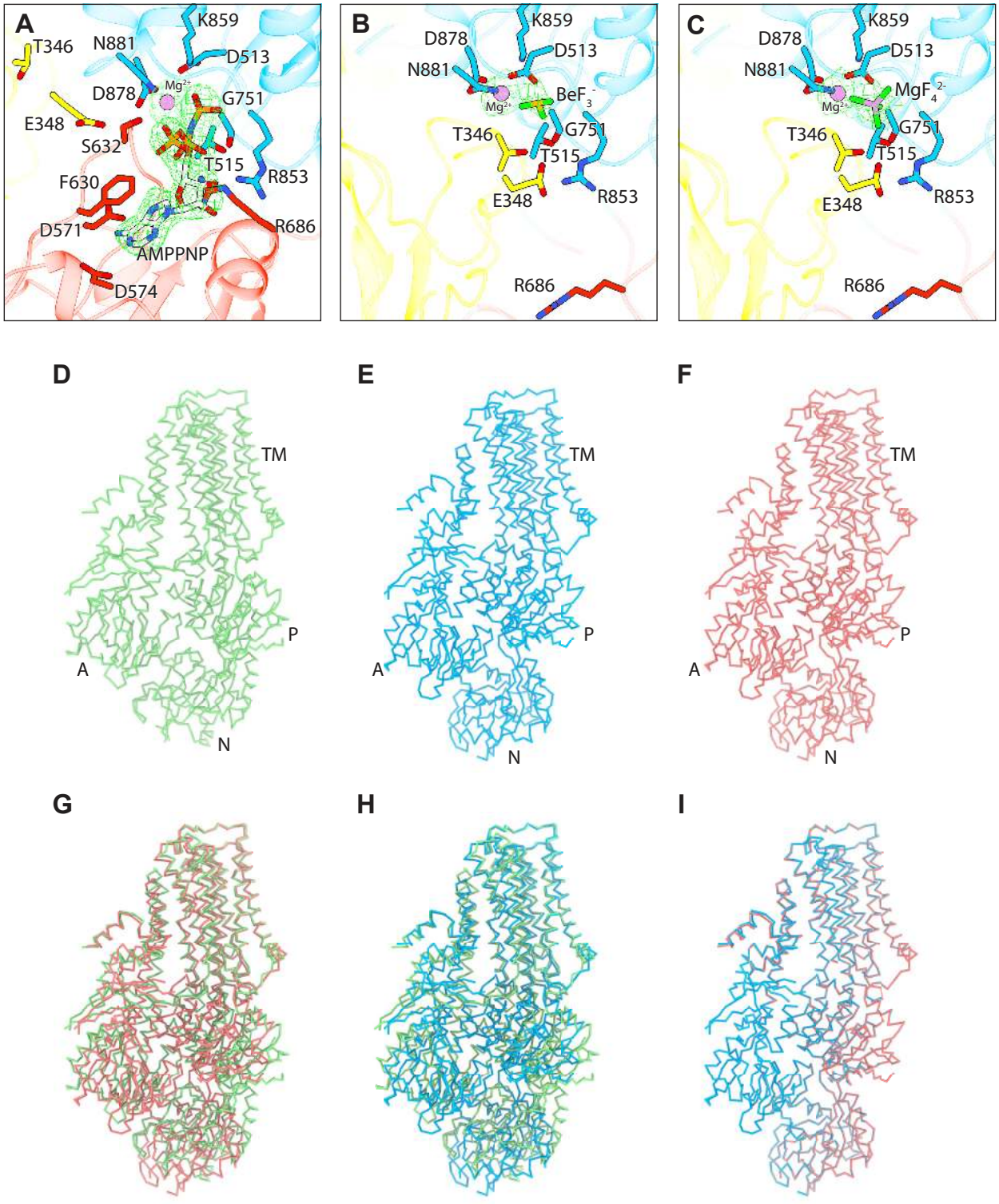

Figure S3. Comparison of hATP13A2 structures, related to Figures 1, 2, and 7.

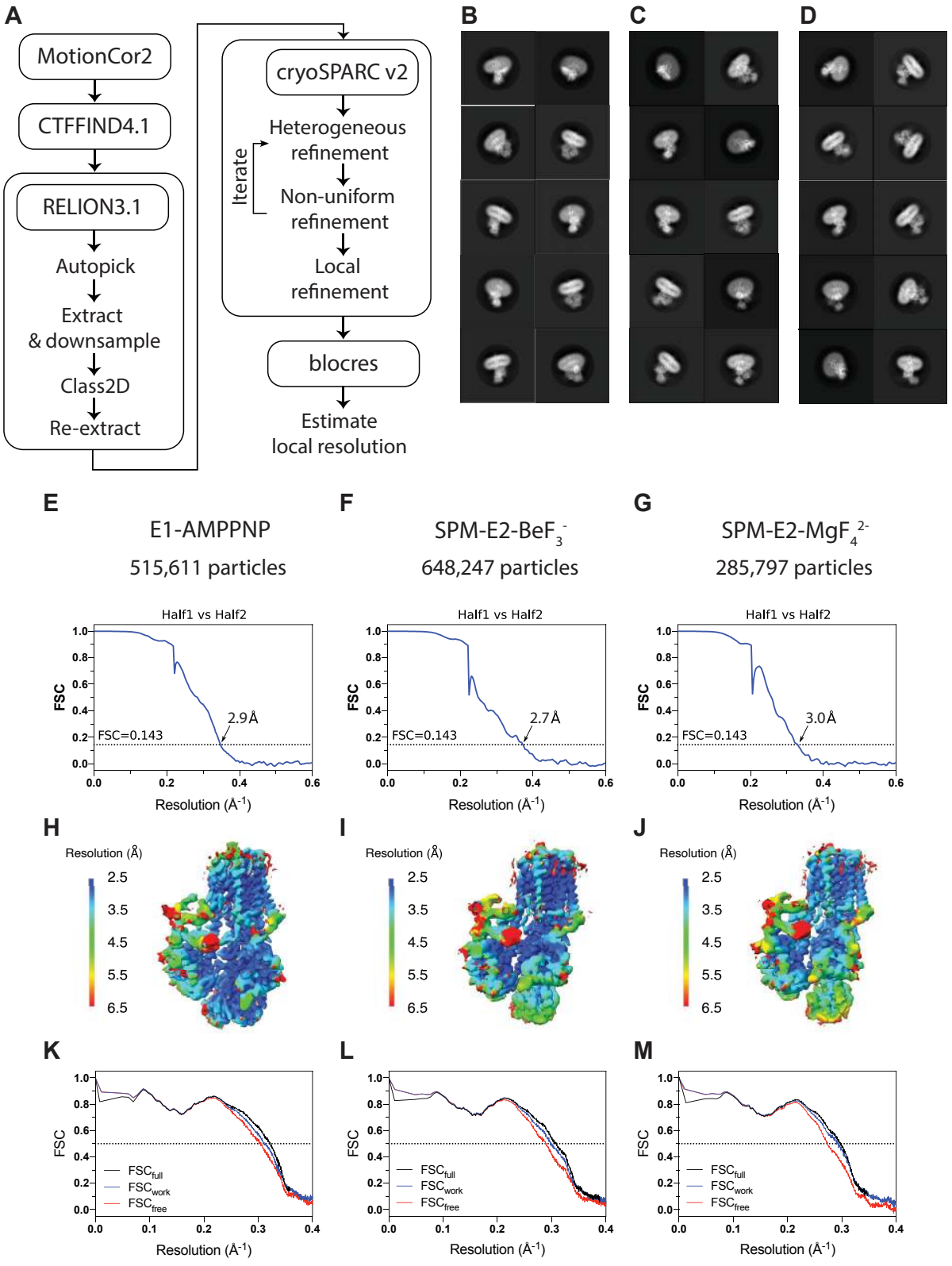

Figure S4. Image processing and resolution estimates, related to Figures 1, 2, 3, and 4.

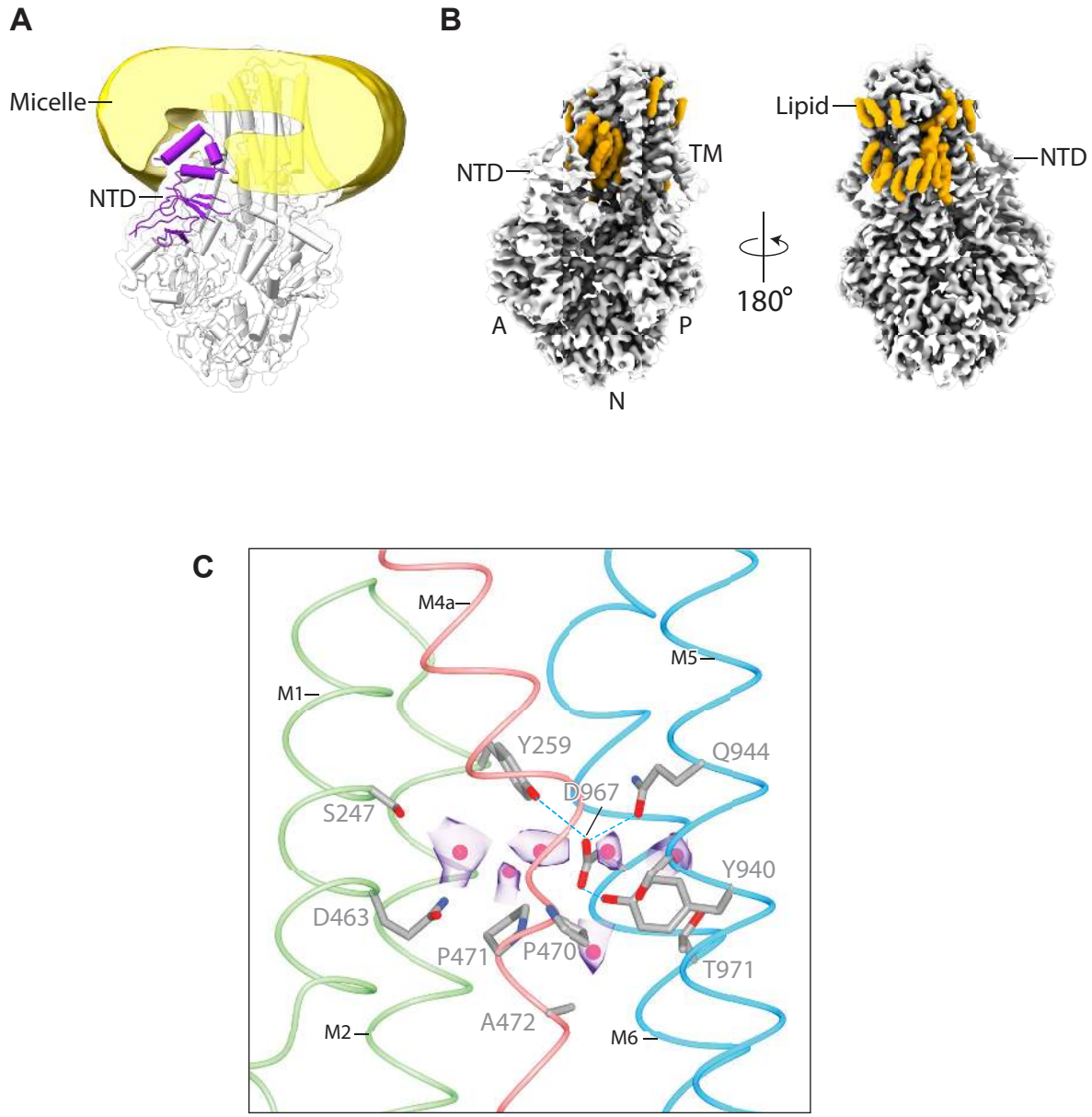

Figure S5. The lipid embedded NTD and the occlusion chamber in the E1-AMPPNP structure, related to Figures 1, 2, and 3.

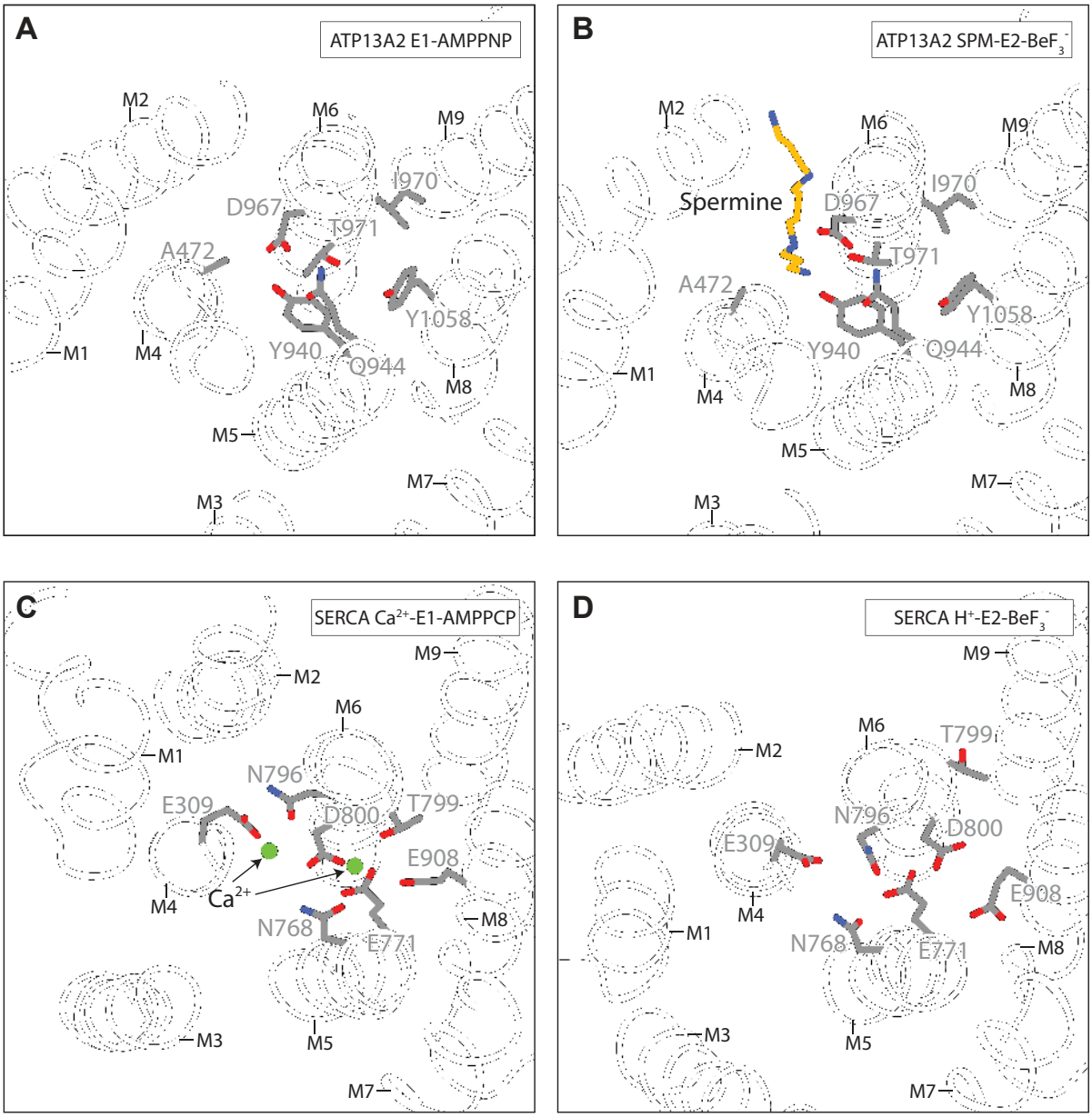

Figure S6. Comparison of SERCA and hATP13A2 structures, related to Figure, related to Figures 3, 4, and 7.

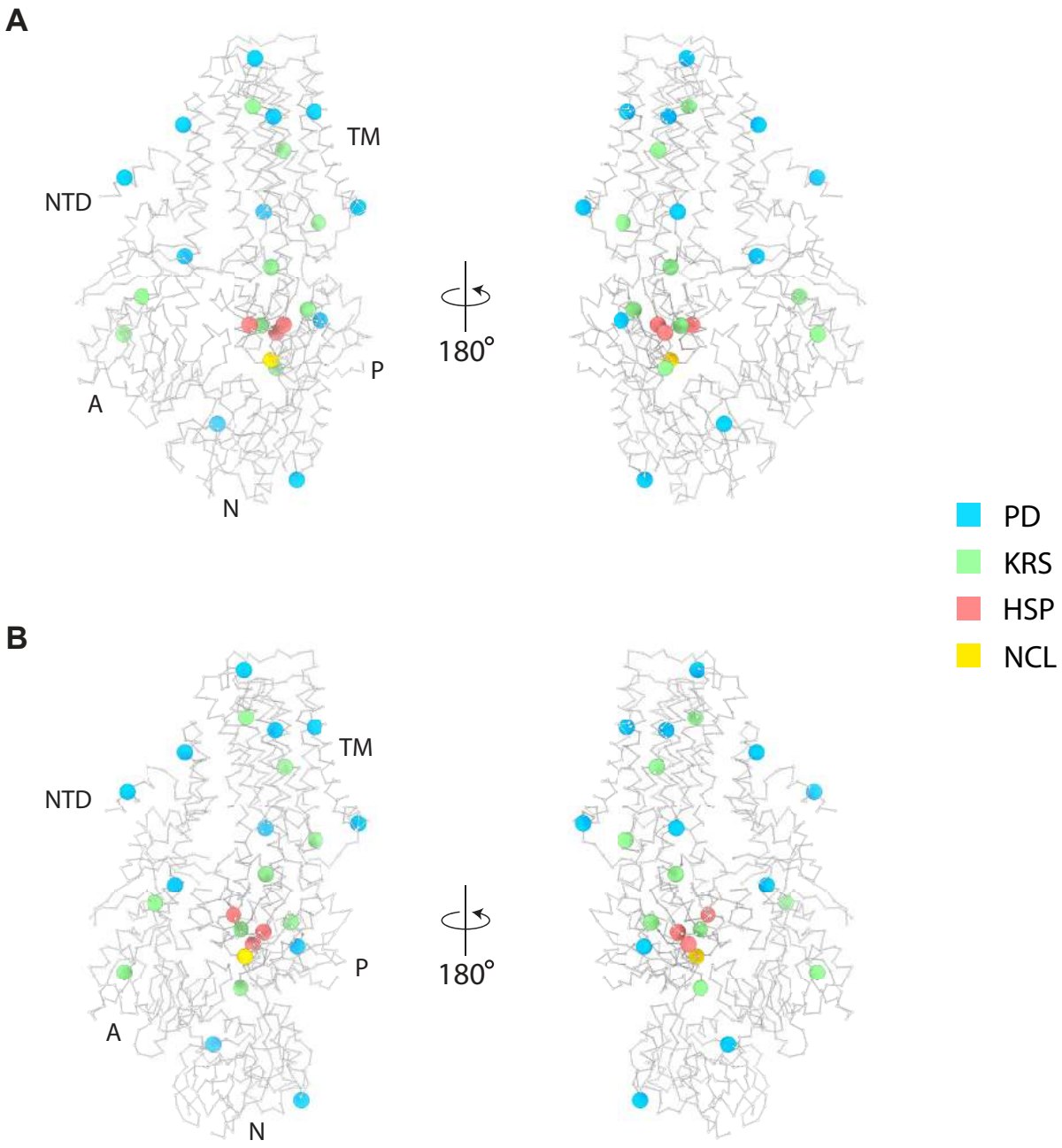

Figure S7. Disease-associated mutations in human ATP13A2, related to Figure 1, 3 and 7.

Table S1. Data collection and refinement statistics, related to Figures 1, 2, 3, 4, 5, 6, and 7

	E1-AMPPNP	SPM-E2-BeF_3^-	SPM-E2-MgF_4^{2-}
Data acquisition			
Microscope	Titan Krios	Titan Krios	Titan Krios
Voltage (kV)	300	300	300
Camera	Gatan K3 Summit	Gatan K3 Summit	Gatan K3 Summit
Camera mode	Super-resolution	Super-resolution	Super-resolution
Defocus range (μm)	0.8 to 1.6	0.3 to 1.3	0.3 to 1.3
Pixel size (Å)	0.830 (super-	0.830 (super-	0.830 (super-
Movies	7,969	18,231	7,336
Frames/movie	70	60	60
Total electron dose	76	65	65
Exposure time (s)	3.5	3.0	3.0
Dose rate (e^-/pixel/s)	15	15	15
Reconstruction			
Software	cryoSPARC v2	cryoSPARC v2	cryoSPARC v2
Symmetry	C1	C1	C1
Initial Particle number	740,626	1,368,235	466,778
Final Particle number	515,611	648,247	285,797
Resolution (masked, Å)	2.9	2.7	3.0
Model statistics			
Residues built	1046/1180	1000/1180	1000/1180
Map CC (masked)	0.78	0.76	0.73
Cβ outliers	0	0	0
Molprobity score	1.66	1.58	1.60
Clash score	4.19	4.19	4.45
Rama-Z score (whole)	0.36	0.04	0.03
Ramachandran			
Favored (%)	92.73	94.47	94.88
Allowed (%)	7.27	5.53	5.12
Outliers (%)	0.00	0.00	0.00
RMS deviations			
Bond length	0.004	0.004	0.006
Bond angles	0.771	0.882	1.144